

CHAPTER 1

PROGRESS IN ASYMMETRIC RESONANT CAVITIES: USING SHAPE AS A DESIGN PARAMETER IN DIELECTRIC MICROCAVITY LASERS

H. G. L. Schwefel, H. E. Tureci, A. Douglas Stone and R. K. Chang

*Department of Applied Physics, Yale University,
P.O. Box 208284, New Haven, CT 06520, USA*

We report on progress in developing optical microresonators and microlasers based on deformations of dielectric spheres and cylinders. We review the different semiconductor and polymer dye microlasers which have been developed and demonstrated using this approach. All the lasers exhibit highly directional emission despite the presence of ray chaos in the system. Lasing has been demonstrated using both optical pumping and electrical pumping in the case of InGaP quantum cascade lasers and very recently in GaN MQW lasers. Lasing modes based on stable and unstable periodic orbits have been found as well as modes based on chaotic whispering gallery orbits; the lasing mode depending on the material, shape and index of refraction. The lasing from modes based on unstable orbits dominated for certain shapes in the GaN cylinder lasers, and is related to the “scarred” states known from quantum chaos theory. Extreme sensitivity of the emission pattern to small shape differences has been demonstrated in the polymer microlasers. Large increases in output power due to optimization of the resonator shape has been demonstrated, most notably in the quantum cascade “bowtie” lasers. Efficient numerical approaches have been developed to allow rapid calculation of the resonant modes and their directional emission patterns for general resonator shapes. These are necessary because the lasing modes are not usually amenable to standard analytic techniques such as Gaussian optical or eikonal theory. Theoretical analysis of the directional emission from polymer lasers has shown that highly directional emission is compatible with strongly chaotic ray dynamics due to the non-random character of the short-term dynamics. Very recently uni-directional emission and electrical pumping have been demonstrated in the GaN MQW system using a spiral-shaped resonator design, bringing this general approach in which shape is used as a design parameter closer to useful applications.

1. Introduction

1.1. Overview

Microresonators based on spherical, cylindrical and disk-shaped dielectrics have been studied for applications to lasers and integrated optical devices for at least two decades.^{1,2,3} These devices exploit the (nearly) total internal reflection which confines whispering gallery modes of such structures and leads to high-Q resonances. However obtaining useful output from such devices, both in terms of lasing power and in terms of controllable directional out-coupling has always been challenging due to their intrinsic isotropy and the fact that out-coupling is typically dominated by random features such as surface roughness. Nine years ago Nöckel, Stone and Chang⁴ proposed that smooth deformations of such resonators, which they termed *asymmetric resonant cavities* (ARCs), could achieve both usefully high-Q modes and controlled out-coupling which might be optimized by varying the shape as a design parameter. In the previous volume of this series the basic physical concepts and theory behind ARCs were presented along with very preliminary experimental results obtained from deformed spherical microdroplet lasers.⁵ The ARC concept is of theoretical interest because such resonators are examples of wave-chaotic systems, similar to systems studied in the field of quantum chaos.⁶ The motion of a light ray confined in such a resonator is in many cases chaotic in the technical sense that this motion exhibits exponential sensitivity to small differences in initial conditions; as a result the analysis of such resonators can be related to a well-known class of problems in non-linear physics, that of classical and quantum billiards, as discussed in detail in the initial and subsequent work.^{5,6} Since that initial work at least four different realizations of semiconductor ARC lasers have been developed and studied,^{7,8,9,10,11} as have polymer ARC dye lasers.¹² We will review much of that experimental work in the current chapter. Overall this work has deepened our understanding of wave-chaotic resonators and of using shape as a design parameter in optimizing the performance of microresonators. It has also shown that a number of the assumptions of the initial theoretical work have a limited range of validity and that the properties of these resonators are more diverse and complex than initially anticipated.

To summarize the major new results prior to a detailed exposition:

- One can get highly directional emission from smoothly-deformed (ARC) resonators and also from dielectric resonators with abrupt

deformations from circular symmetry (such as the “spiral” laser discussed below.¹³)

- The lasing modes can have a wide range of geometries and properties: these include chaotic whispering gallery modes, modes based on stable periodic orbits, modes based on unstable periodic orbits (“scarred modes”), and chiral whispering gallery modes (modes strongly favoring one sense of rotation).
- Fully chaotic laser resonators (i.e. those with no stable or marginally stable periodic orbits) can still have highly directional emission due to non-random short-term dynamics.
- The high emission directions are extremely sensitive to the shape of the resonator and its index of refraction in a manner which can be understood by analysis of the phase space for ray motion.
- The lasing mode selected also depends on the shape of the resonator and its index of refraction and gain, however in a manner which is not yet fully understood.
- Theoretical analysis of the passive cavity based on efficient new computational algorithms allows one to identify the lasing mode based on comparison with experiment.
- Deformation of the resonator from circular symmetry can lead to a substantial improvement in the peak power output (several orders of magnitude) for lasing media with the same gain.
- An efficient electrically-pumped microlaser in the GaN materials system with uni-directional emission has been demonstrated using the shape design approach.

We will review the experimental and theoretical work leading to these conclusions below.

2. Review of theoretical techniques

2.1. Background

The use of mirror-based “open” resonators was a key step in the development which led from the maser to the laser. The theory of mirror-based resonators is well developed for standard Fabry-Perot and ring resonator configurations, and in itself fills several hundred pages in standard textbooks.¹⁴ In such a case the location of the mirrors defines an optical path which leads to high-Q resonances and feedback (in the case of an active cavity); in most cases this path is a simple linear motion between parallel mirrors. The shape and spacing of the mirrors defines the stability of the ray motion between

them and other properties of the output beam. Another important type of resonator for semiconductor lasers is based on distributed Bragg reflectors, dielectric layers which are spaced to cause destructive interference, hence acting as efficient mirrors for light at normal incidence. Again for this case the light path is simply a linear back and forth motion with reflection at normal incidence. The ray motion in such resonators can be fitted into the general framework of paraxial optics and “ABCD” matrices which describe propagation through a series of optical elements such as lenses and mirrors. This ray description is easily translated into solutions of the wave equation using the methods of Gaussian optics if the ray path is stable and periodic.^{14,15} In contrast, dielectric resonators allow trapping of many different light trajectories for long times and mode geometries which are much more complex. The paradigm of a simple correspondence between a periodic ray orbit and a set of resonant modes of the cavity fails. Even for the case of simple whispering gallery orbits of a perfectly-reflecting cylinder the resonant modes are determined by zeros of the Bessel function which are not in general equally spaced in wavevector as are the modes of resonances based on stable periodic ray orbits. However in this case of a perfectly circular cylinder it is possible to write down approximate analytic solutions of the wave equation based on ray trajectories using eikonal theory.¹⁶ A much more fundamental problem arises in generically deformed cylinders. In this case both of the familiar analytic methods for treating resonators, Gaussian optics and eikonal theory, are simply not applicable to a large fraction of the spectrum due to the possibility of chaotic ray motion. This is a crucial point which does not seem to have been appreciated anywhere in the optics literature: *all conventional methods of geometric or Gaussian optics fail in a resonator which has chaotic ray motion.* We shall explain the origin of this failure shortly. Several analytic methods for making short-wavelength approximations to such chaotic wave problems have been developed in the recent past for the Schrödinger equation in the study of “quantum chaos”, but these methods do not allow one to construct *individual* solutions as one can for regular ray motion using Gaussian or eikonal methods. Therefore it is particularly important to have efficient numerical approaches to these problems; we present such an approach and some representative results from it below.

2.2. Failure of conventional geometric optics

We begin by explaining how the presence of ray chaos leads to the failure of conventional methods of eikonal theory and Gaussian optics for treating the wave equation in a dielectric resonator analytically in the short-wavelength limit. Both eikonal theory and Gaussian optics apply only in the limit in which the wavelength of the modes is much less than typical geometric features of the resonator, such as relevant chord lengths and radii of curvature of the boundary. Gaussian optics, based on the parabolic equation method,^{15,17} only allows one to determine the modes of the resonator that are localized in the vicinity of isolated *stable* periodic orbits, and may be regarded as an improved version of the eikonal method; the latter method works both for such stable orbit modes and for a more general class of marginally stable modes to be discussed below. Hence we will focus mainly on the failure of eikonal methods in our initial discussion and at the end explain the relationship to Gaussian optics. As noted, both methods are based on approximations to the exact wave equation which are only valid when $kR \gg 1$, where we shall use R to refer to a typical linear dimension of the resonator and assume all radii of curvature are of order R . It should also be noted that all of the problems we will be interested in correspond to non-separable boundary conditions on the wave equation and hence cannot be solved exactly by separation of variables or by any other known analytic method. Therefore short-wavelength approximations are the natural method to use to attempt a solution. For almost all microresonators that have been studied experimentally the resonator is indeed in the limit $kR \gg 1$ which would appear to be sufficient to validate such approaches. Nonetheless the methods fail; a more detailed version of the argument explaining this failure has been given recently in Ref. 18. Interestingly, the basic argument goes back to a little-known paper by Einstein in 1917.¹⁹

For simplicity, throughout this article we will be dealing with the resonances of an infinite uniform dielectric rod of index of refraction n and arbitrary cross-section ∂D , and will focus on planar solutions for which the z-component of conserved momentum, $k_z = 0$. For this system the solutions have either the electric field (TM solution) or magnetic field (TE solution) solely in the the z-direction and the amplitude of this field $E_z(x, y)$, $B_z(x, y)$ satisfies the scalar wave (Helmholtz) equation:

$$(\nabla^2 + n^2 k^2)\psi(x, y) = 0. \quad (1)$$

Here $\psi(x, y)$ refers to the electric or magnetic field for the TM, TE cases respectively and we assume a harmonic time-dependence with frequency

$\omega = ck$. This is a reasonable model for a micropillar resonator with a

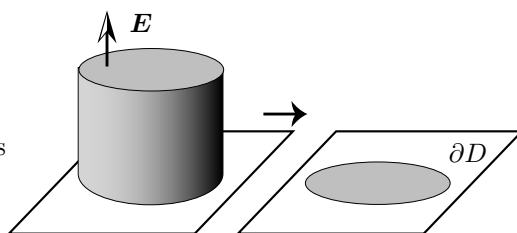


Fig. 1. Illustration of the reduction of the Maxwell equation for an infinite dielectric rod of general cross-section to the 2D Helmholtz equation for the TM case (E field parallel to axis) and $k_{\parallel} = k_z = 0$.

large aspect ratio of height to radius. The highest Q modes will be the planar modes which do not escape through the top and bottom. The correct boundary conditions for the problem are the continuity of ψ and $\partial_{\hat{n}}\psi$ across the boundary, where the wavevector changes from nk (inside) to k (outside). These conditions will describe the physics of near total internal reflection and Fresnel refraction and reflection at the interface. Below we will present briefly a new numerical method to solve Eq. (1) with these boundary conditions very efficiently, and we will show many numerical results obtained with this method. However to illustrate why such a problem is not amenable to analytic description using ray optical or eikonal methods, it is sufficient and simpler to consider perfectly reflecting boundary conditions corresponding to $\psi = 0$ everywhere on the boundary. It can be straightforwardly shown that dielectric matching boundary conditions do not remove the fundamental limitation which we now describe.²⁰ For the perfectly reflecting case we need only consider $\psi(x, y)$ inside the domain D of uniform index n and hence we can set $n = 1$ for convenience.

The eikonal method consists of attempting an asymptotic solution of Eq. (1) (now with $n = 1$) of the form

$$\psi(x, y) = A(x, y)e^{ikS(x, y)} \quad (2)$$

where $kR \gg 1$ and S, A are real functions independent of k and $A \equiv A_0$ is the first term in a power series in k^{-1} . This ansatz is used in Eq. (1) and terms of lower order in k^{-1} are initially neglected to yield the eikonal and transport equations:

$$(\nabla S)^2 = n^2(x, y) \quad (3)$$

$$2\nabla S \cdot \nabla A + A\nabla^2 S = 0 \quad (4)$$

for $S(x, y)$ and $A(x, y)$. $S(x, y)$ is a scalar field whose level curves describe the “wavefronts” of the solution which are assumed to be slowly varying in space, as the factor k in the exponent takes care of the rapid variation on the scale of the wavelength; the unit vector field ∇S describes the direction of ray motion at a given wavefront. For a uniform medium a ray originating on one wavefront must “move” in a straight line, even though the wavefronts themselves cannot be straight lines if the confining boundary of the medium is curved. For the current discussion the properties of the amplitude A and the transport equation which determines its properties once S is known are not crucial except for one property. The Dirichlet boundary conditions we are assuming require that ψ vanish on the boundary; one can easily see that if one attempts to satisfy this by setting $A = 0$ on the boundary that the transport equation will give $A = 0$ everywhere in the domain D . Thus the boundary conditions must be satisfied by the cancellation of two or more terms of the form Eq. (2) and for eikonal solutions within a bounded region the solution must have the form:

$$\psi(x, y) = \sum_n^N A_n(x, y) e^{ikS_n(x, y)} \quad (5)$$

where $N \geq 2$. Thus any eikonal solution must involve at least $N \geq 2$ sets of wavefronts defined by $S_1(x, y), S_2(x, y) \dots S_N(x, y)$ and N sets of rays determined by $\nabla S_1, \nabla S_2 \dots \nabla S_N$. A further implication of the boundary conditions is that the functions S_n must be pairwise equal on the boundary and their gradients on the boundary must satisfy “specular reflection” pairwise, i.e. $\hat{n} \cdot \nabla S_1 = -\hat{n} \cdot \nabla S_2$ and so on, for each pair. The key question raised by these constraints is whether such a set of wavefronts and associated ray vector fields can be consistently constructed for a given boundary ∂D ?

We can reduce the previous question to a very specific question about ray dynamics in a perfectly reflecting “billiard” (the term for the problem of a point mass specularly reflecting from hard boundaries in two dimension). Modern research in non-linear dynamics then allows us to answer this question generically. Consider a point $r_0 = (x_0, y_0)$ in the domain which is arbitrary except that the solution we are seeking $\psi(x_0, y_0)$ and $\nabla \psi(x_0, y_0)$ are non-zero at that point and in a small neighborhood around it. Then at this point there are N different ray directions defined by $\nabla S_1, \nabla S_2 \dots$. Choose one of these direction e.g. ∇S_1 and follow it in a straight line to the boundary (for a uniform medium this line will run exactly along ∇S_1 as noted). The specular reflection boundary condition just mentioned implies

that upon reaching the boundary and specularly reflecting this ray the new direction corresponds to a ray of another of the vector fields, e.g. ∇S_2 . We can thus be assured that each ray we follow from (x_0, y_0) will stay on one of the allowed ray directions determined by the N sets of wavefronts defined by the S_n . By a well-known property of classical mechanics in a bounded system this ray must eventually return to the neighborhood of (x_0, y_0) over and over. If such eikonal solutions exist, such a ray by assumption must pass through this neighborhood each time in one of the N allowed ray directions defined at r_0 . However this is a special dynamical behavior which need not hold. It turns out that three situations are possible.

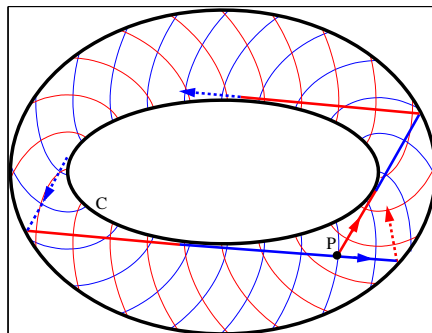


Fig. 2. The wavefronts and the corresponding set of rays generated by an elliptic boundary. There are two sets of wavefronts $S_1 = \text{const.}$ and $S_2 = \text{const.}$ (and their corresponding rays), drawn in red and blue respectively, which together satisfy the boundary conditions on the elliptic boundary, provided the caustic curve and the wavevector k is chosen according to the EBK quantization conditions. In this figure, a (red) ray is started at point P , towards the caustic C . Subsequent iterations according to the specular reflection rule generate rays which are always tangent to the elliptic caustic C . Irrespective of the starting position P , there can be one and only one other return direction (blue) at P . This is the unique hallmark of integrable ray motion. Note that we consider only one sense of rotation for rays; the other sense of rotation is disjoint from this set (ray dynamics conserves the “chirality”) and the corresponding wavefronts generate a second linearly independent eikonal solution.

- If the ray dynamics of this system allows this special behavior to occur for *all* initial ray choices at r_0 , then we can construct a full spectrum of consistent eikonal solutions with a finite number of terms N . The quantization condition on k arises from requiring the single valuedness of ψ at each point r_0 ; an elegant means to implement this condition is described in the classic paper by Keller

and Rubinow¹⁶ following the suggestion by Einstein. Such cases are referred to as *integrable*. A solvable example for which the method works is an elliptical boundary. The relevant ray fields and wavefronts are illustrated in Fig. 2.

- If the number of ray return directions tends to infinity as $t \rightarrow \infty$ for all choices of initial ray directions at r_0 then no consistent eikonal solutions exists. This will be the case for systems which are completely chaotic.
- If the number of ray return directions at r_0 is sometimes finite and sometimes tends to infinity depending upon the initial ray direction then the system is referred to as *mixed* and in principle it will be possible to find eikonal solutions for only a subset of the spectrum. In practice, for the mixed case, eikonal solutions are only easily found near stable periodic orbits and quasi-periodic KAM tori.

Modern research in non-linear dynamics tells us that the third, mixed case is the generic case. For example, any smooth deformation of a circular boundary which is not exactly elliptical will lead to the mixed case. We shall see below that a simple smooth quadrupolar deformation of the circle generates a very high degree of chaos and makes it impossible in practice to use the eikonal method except near the few remaining short stable periodic orbits.

To summarize the basic point of the previous argument: in order to generate a resonant mode within a given boundary one has to be able to launch a finite set of waves from each point which bounce around in the cavity and return so as to constructively interfere and form a standing wave. Only certain very special symmetric boundaries allow one to do this from all points in the cavity using waves propagating in an arbitrary direction. When it is not possible to do this the eikonal method does not apply.

It is important to realize that even when the eikonal approach fails there exists the same average density of modes as for the more symmetric shapes; this is guaranteed by various theorems, such as the Weyl theorem.²¹ However these solutions do not have wavefronts that are smooth on the scale of the wavelength and hence cannot be obtained by the asymptotic (eikonal) method.

Having explained this fundamental limitation on the use of the eikonal method for chaotic or mixed systems, we now briefly discuss how similar considerations apply to the method of Gaussian optics. In this method we search for solutions localized near periodic ray orbits of the problem. It

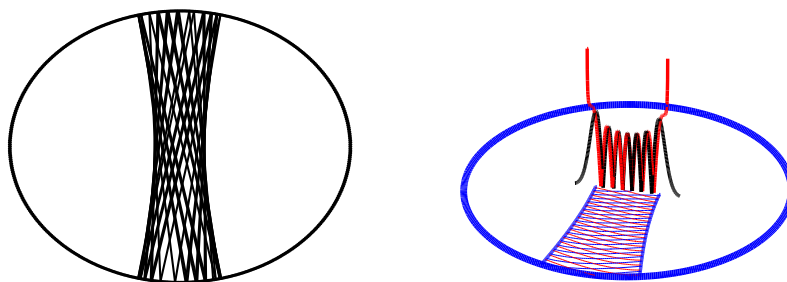


Fig. 3. (a) Real space plot of the simulation of a ray initially started in the stable bouncing ball region of an elliptical billiard of deformation $\epsilon = 0.12$. (b) The EBK wavefronts corresponding to a bouncing ball mode generated by an elliptic boundary. For simplicity we have only plotted two of the four sets of the wavefronts above the major axis. The other two sets of wavefronts represent the time-reversed motion. We also plot the transverse variation of the resulting eikonal solution in red. Note that this solution has a singularity on its hyperbolic caustic. In black is plotted the Gaussian-optical approximation to the bouncing ball mode, which is uniformly valid over the whole transverse cross-section of the wavefield.

is helpful to note that such localized solutions can always be found using the eikonal method as well. The eikonal solutions near stable periodic orbits are of the type found near the stable two-bounce orbit of the ellipse billiard illustrated in Fig. 3. A ray emanating from a point in the neighborhood of the periodic orbit moving in approximately the same direction will bounce back and forth in the vicinity of the orbit indefinitely; each segment of its trajectory will be tangent to a hyperbolic caustic curve and hence will satisfy the property of only returning to the initial point in four possible directions. Therefore we can build up consistent wavefronts leading to standing waves in the vicinity of the periodic orbit and quantize the wavevector by imposing periodicity. One finds the following quantization rule:

$$kL = 2\pi m + (q + 1/2)\phi + \pi \quad (6)$$

where L is the total length of the two-bounce orbit, m, q are integers, ϕ is the phase velocity of the orbit as it rotates around the fixed point, and is directly obtainable in terms of the radius of curvature at the bounce points and length of the orbit. The additional phase π is the specific value for the two-bounce orbit with Dirichlet boundary conditions of the Maslov phase which appears for any such periodic orbit; the general value of this phase for an arbitrary periodic orbit depends on the boundary conditions, number of bounces and topological properties of the orbit.¹⁵ Thus we have

two characteristic constant modes spacings: the longitudinal mode spacing or free spectral range (FSR), $\Delta k_L = 2\pi/L$ and the transverse mode spacing $\Delta k_T = \phi/L$. This quantization rule, obtained from the eikonal method,¹⁶ is identical to that obtained by the Gaussian optics method¹⁵ when specialized to this two-bounce case. The actual solution $\psi(x, y)$ one constructs via the eikonal method will however have a diverging amplitude at the caustic of the ray motion, which is a standard limitation of the eikonal method, analogous to the well-known divergence of WKB solutions at a classical turning point.

The Gaussian optical solution is somewhat different as it begins from the reduction of the wave equation to a parabolic differential equation in the large k limit, which it then solves by the Gaussian ansatz. The solutions, while having the same quantized k -values as the eikonal solution, provide a more accurate description of the mode in space, which does not diverge at the caustic. Instead the Gaussian solution has a finite peak at the caustic and is well-defined everywhere in space (see Fig. 3(b)). In fact the Gaussian optics method can be regarded as an improved eikonal ansatz in which the phase function $S(x, y)$ is complex (something we excluded earlier) leading to a uniform approximation which allows continuation across the caustic (or classical turning point).

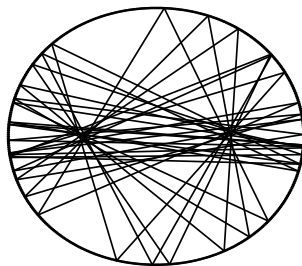


Fig. 4. Realspace plot of the simulation of a ray initially started close to the long diameter of the quadrupole of deformation $\epsilon = 0.07$.

However the Gaussian approach does *not* provide a solution to the fundamental problem of quantizing chaotic motion. Chaotic motion occurs in the vicinity of *unstable* periodic orbits. A ray emanating from a point near an unstable periodic orbit will not remain near that orbit, confined by a caustic. Instead it will propagate far away from the original orbit and generically will return to the original neighborhood in a random direction (see Fig. 4). Therefore both eikonal and Gaussian methods will fail here. Technically, in the derivation of the Gaussian solutions, stability of the associated

periodic orbit is required in order for the transverse behavior to have a Gaussian decay; if the orbit is unstable the transverse solution oscillates without decay and this violates the assumptions one makes in defining the approximation.¹⁵ Thus, like eikonal theory, Gaussian optics fails to provide an analytic description of modes associated with regions of chaotic ray motion.

However in generic (mixed) systems there always exist stable periodic orbits and the Gaussian method is a convenient analytic method to extract the *subset* of the resonant modes which *are* associated with stable periodic orbits. The application to dielectric resonators has been worked out in detail in reference 15 and some results using the method applied to stable “bowtie” resonances are reviewed in Section (5.1) below.

2.3. *The phase space method for ray dynamics*

In the previous section we argued for the failure of analytic short-wavelength approximations to describe a finite fraction of the spectrum in generic resonators. We based the argument on modern results describing the motion of a point mass moving freely within a perfectly reflecting two-dimensional boundary or billiard, which is mathematically identical to ray motion within a closed resonator. In introducing the phase space methods for treating such systems we will initially treat only this closed case; afterwards we will note the change in the picture necessitated by the possibility of ray escape. The crucial result we quoted was that for a billiard which is a smooth deformation of a circle the ray dynamics is mixed, meaning that some initial conditions lead to regular motion tangent to a caustic curve and other initial conditions lead to chaotic motion which is pseudo-random at long times. This statement has an important meaning in phase space. The phase space for a point mass in two dimensions is four dimensional, but as the energy is assumed conserved, any given trajectory must lie on a three-dimensional subspace of phase space. If there is a second constant of the motion, such as the angular momentum for the circle (or its generalization for the ellipse), then each trajectory lies on a two-dimensional subspace of the constant energy surface with the topology of a torus. However if there is no second global constant of motion, as for generic deformations of a circular billiard, then the results of Kolmogorov-Arnold-Moser (KAM) theory^{22,23} imply that for such mixed systems some initial conditions result in trajectories which explore a finite fraction of the three-dimensional constant energy surface and other initial conditions result in trajectories which remain on

a two-dimensional subspace of this surface with the topology of a torus (a “KAM” torus). To get an overall view of the phase space dynamics for a given shape it is very convenient to use the tool of the Poincaré surface of section, introduced in this context some time ago,⁵ which we now briefly review.

As the behavior we are describing is known from KAM theory to be generic for smooth deformations of the circle we will restrict ourselves in the subsequent discussion to the simple example of the quadrupole billiard described by the boundary shape:

$$R(\phi) = 1 + \epsilon \cos 2\phi \quad (7)$$

which in the zero deformation limit $\epsilon = 0$ reduces to a circular billiard and is integrable. Variation of the parameter ϵ starting from zero induces a transition to chaos, meaning a fraction of finite measure of the initial conditions lead to chaotic motion. This measure increases with increasing deformation but does not reach unity for any known smooth deformation (there are non-smooth deformations of a circle, such as the stadium billiard for which the fraction is known to be unity). Real-space ray-tracing is not helpful to analyze this transition since chaotic trajectories tend to fill the entire real-space even if they do not fill the constant energy surface uniformly; thus much of the structure is not visible. Instead, to visualize the increase in the chaotic fraction of phase space we image a set of trajectories each time they hit the boundary and plot the result in a two-dimensional graph known as the surface of section^{21,24} (see Fig. 5).

In this two-dimensional phase-space representation, the internal ray motion is conveniently parametrized by recording the pair of numbers $(\phi_i, \sin \chi_i)$ at each reflection i , where ϕ_i is the polar angle denoting the position of the i th reflection on the boundary and $\sin \chi_i$ is the corresponding angle of incidence of the ray at that position (see Fig. 5). Each initial point is then evolved in time through the iteration of the SOS map $i \rightarrow i+1$, resulting in two general classes of distributions. If the iteration results in a one-dimensional distribution (an *invariant curve*), the motion represented is *regular*. On the other hand exploration of a two-dimensional region is the signature of *chaotic* motion which covers a finite fraction of the constant energy surface in phase space.

The transition to ray chaos in the quadrupole billiard is illustrated in Fig. 6. At zero deformation the conservation of $\sin \chi$ results in straight line trajectories throughout the SOS and we have globally regular motion. These are the well-known whispering gallery (WG) orbits. As the deformation is

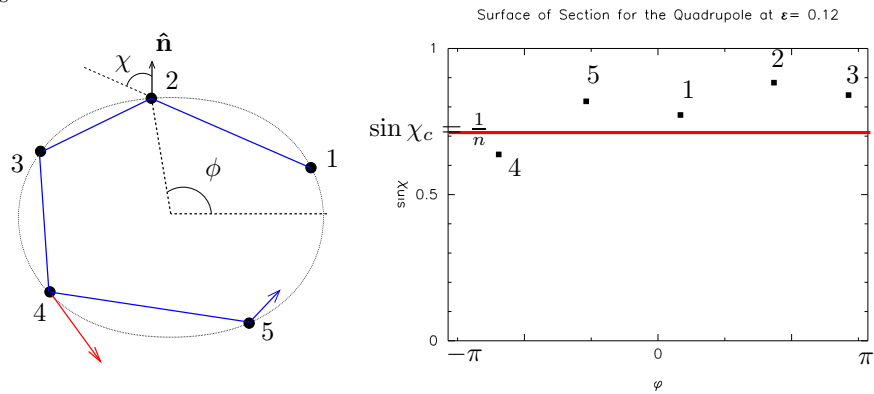


Fig. 5. The construction of the surface of section plot. Each reflection from the boundary is represented by a point in the SOS recording the angular position of the bounce on the boundary (ϕ) and the angle of incidence with respect to the local outward pointing normal ($\sin \chi$). For a standard dynamical billiard there is perfect specular reflection and no escape. For “dielectric billiards” if $\sin \chi > \sin \chi_c > 1/n$, total internal reflection takes place, but both refraction and reflection according to Fresnel’s law results when a bounce point (bounce #4 in the figure) falls below the “critical line” (shown in red) $\sin \chi > \sin \chi_c$. Note that $\sin \chi < 0$ correspond to clockwise sense of circulation. We do not plot the $\sin \chi < 0$ region as the SOS has reflection symmetry. Below we will plot the SOS for ideal billiards without escape unless we otherwise specify.

increased (see Fig. 6) chaotic motion appears (the areas of scattered points in Fig. 6) and a given initial condition explores a larger range of values of $\sin \chi$. Simultaneously, islands of stable motion emerge (closed curves in Fig. 6), but there also exist extended “KAM curves” (the SOS projection of KAM tori)²³ (open curves in Fig. 6), which describe a deformed WG-like motion close to the boundary. These islands and KAM curves cannot be crossed by chaotic trajectories in the SOS. As the transition to chaos occurs, a crucial role is played by the *periodic orbits* (POs), which appear as fixed points of the SOS map. The local structure of the islands and chaotic layers can be understood through the periodic orbits which they contain. Thus, the center of each island contains a stable fixed point, and close to each stable fixed point the invariant curves form a family of rotated ellipses. The Birkhoff fixed point theorem²⁴ guarantees that each stable fixed point has an unstable partner, which resides on the intersection of separatrix curves surrounding the elliptic manifolds. Chaotic motion sets in at separatrix regions first, and with increasing deformation pervades larger and larger regions of the SOS. Already at $\epsilon = 0.1$, much of the phase space is chaotic and a typical initial condition in the chaotic sea

explores a large range of $\sin \chi$, eventually reversing its sense of rotation. For $\epsilon = 0.18$ the entire SOS above $\sin \chi \approx 0.4$ appears chaotic. There is an important practical implication of these results. For rather smooth shapes and relatively small deformations chaotic motion dominates and the failure of analytic methods for such shapes is a barrier to understanding the spectrum of the corresponding wave problem.

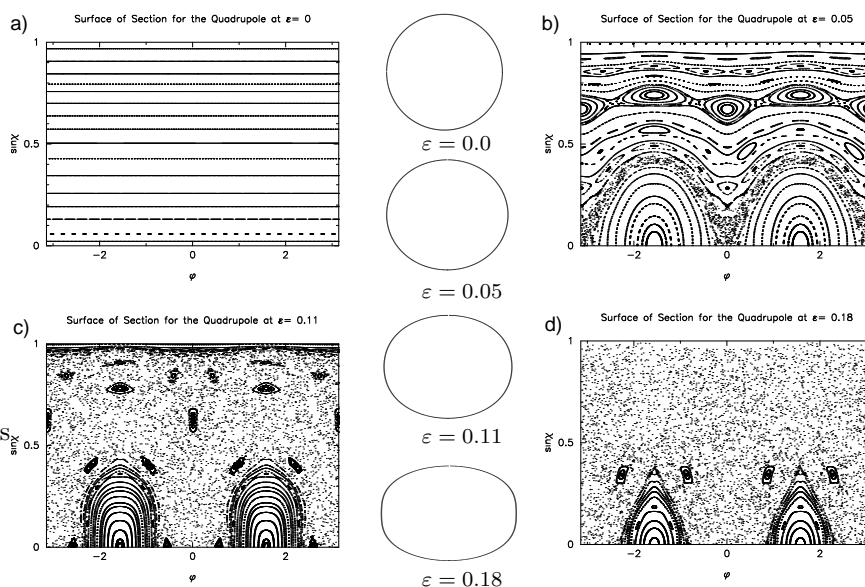


Fig. 6. The SOS of a quadrupole at fractional deformations $\epsilon = 0, 0.05, 0.11, 0.18$. The closed curves and the curves crossing the SOS represent two types of regular motion, motion near a stable periodic orbit and quasi-periodic motion respectively. The regions of scattered points represent chaotic portions of phase space. A single trajectory in this “chaotic component” will explore the entire chaotic region. With increasing deformation the chaotic component of the SOS (scattered points) grows with respect to regular components and is already dominant at 11 % deformation. Note in (b) the separatrix region associated with the two-bounce unstable orbit along the major axis where the transition to chaotic motion sets in first.

We now comment briefly on the relevance of these results for the closed behavior for the dielectric billiards. As we are always assuming $kR \gg 1$ we are in the limit for which ray optics describes a light ray interacting with the dielectric boundary. Therefore internal reflection for light rays hitting with $\sin \chi > 1/n$ is almost total and the closed billiard description for the portion of trajectories which remain for some time in this region of phase space

is quite accurate. However any portion of the trajectory which involves reflection with $\sin \chi < 1/n$ will be subject to refractive escape, typically within a few bounces. Therefore in the context of the analysis of dielectric resonators we introduce a *critical line* $\sin \chi = 1/n$; portions of the SOS below this line are not to be regarded as supporting long-lived resonances even though they might do so in the closed resonator. Typical resonances we will be interested in emit most of their radiation from the vicinity of the critical line as we shall see below. Certain aspects of these resonances can be modeled by following ray bundles in the SOS and allowing rays to escape with the probability given by the Fresnel law when a ray passes below the critical line. The phase space “flow pattern” then determines the directional emission from these resonances as shown in detail in Section (3).

The reason that ray models have some relevance to the wave solutions even in the chaotic case is that even in this case it is possible to associate wave solutions with different regions of phase space and (neglecting interference effects) hence with bundles of rays. In the next sections we will illustrate this fact by formulating the resonance problem and a numerical method for its solution, and then show how such solutions can be projected onto the SOS and interpreted in terms of ray dynamics.

2.4. The resonance problem

We now briefly review the formulation of the exact resonance problem, specializing to an infinite uniform dielectric rod of arbitrary cross-section D . For this geometry the Maxwell equations for the problem reduce to the Helmholtz equation (1) for the E-field (TM), and B-field (TE) polarizations, which we have denoted $\psi(x, y)$, assuming a uniform solution in the z-direction. As also noted the electromagnetic boundary conditions reduce to continuity of ψ and its normal derivative on the boundary ∂D . Assuming the boundary is a smooth deformation of the circle it is convenient to expand the solutions inside and outside the rod in terms of the solutions of the Helmholtz equation at a given wavevector in polar coordinates:

$$\psi_1(r, \phi) = \sum_{m=-\infty}^{\infty} (\alpha_m H_m^+(nkr) + \beta_m H_m^-(nkr)) e^{im\phi} \quad r < R(\phi) \quad (8)$$

$$\psi_2(r, \phi) = \sum_{m=-\infty}^{\infty} (\gamma_m H_m^+(kr) + \delta_m H_m^-(kr)) e^{im\phi} \quad r > R(\phi) \quad (9)$$

where H_m^-, H_m^+ are the incoming and outgoing Hankel functions respectively. If we assume a single incoming wave with unit amplitude for angular mo-

mentum m , the matching conditions are sufficient to find a solution for all k values and the coefficients of the outgoing waves define a unitary S-matrix $S_{m,m'}(k)$. However we are only interested in the special values of k at which a long-lived resonance of the system exists, as these will correspond (approximately) to the emitting modes of the active cavity. We could look for rapid variations in the S-matrix as we vary k , which indicate resonant scattering, but this is inconvenient for various reasons. Instead we define the quasi-bound states as the solutions of this matching problem with no incoming wave from infinity ($\delta_m = 0$ in Eq. (9)). Due to the violation of flux conservation, no such solution exists for real wavevectors k , but a discrete set of solutions exist at complex wavevectors $k = q - i\gamma$, known as the quasi-bound states or quasi-normal modes of the system. Long-lived resonances have $q \gg \gamma$ and the Q-value can be defined as $Q = 2q/\gamma$. After the resonance wavevectors are found, the corresponding mode can also be determined and plotted both within the resonator and in the farfield. The farfield solutions have the unphysical feature that they increase in intensity as $\exp[2\gamma r]$, reflecting the decay from the cavity, but this unphysical dependence does not affect the angular distribution of radiation, which is the farfield quantity we are interested in. Introducing an imaginary part of the index into the problem (representing amplification in the cavity) would lead to solutions for real k with the same angular dependence and no exponential growth at infinity.

An approach to solving this problem termed the ‘‘S-matrix method’’ has been developed over a number of years;^{25,26,20,18} the most recent version of this approach is highly efficient for the specific problem of ARC resonators. The numerical results plotted in the remainder of this paper were all obtained by this method. The approach begins by integrating the matching conditions over the azimuthal angle ϕ with $r = R(\phi)$; this eliminates the spatial dependence and transforms the matching conditions into an infinite set of linear relations for the coefficients $\{\alpha_m\}, \{\beta_m\}, \{\gamma_m\}$. This infinite set of relations can be truncated because for $m \gg nkR$ the corresponding Hankel functions have negligible weight in the cavity. We thus end up with order $2nkR$ linear relations which must be satisfied by the coefficients. These relations and the regularity condition on the solution at the origin yield a determinantal equation for the form:

$$\zeta(k) = \det[1 - \mathcal{S}(k)]. \quad (10)$$

The matrix $\mathcal{S}(k)$ is not the unitary scattering matrix of this problem, but it is nearly unitary for real k ; the complex values of k which make the

determinant zero (eigenvalue of $\mathcal{S} = 1$) are the quasi-bound wavevectors we seek. Once they are known the coefficients $\{\alpha_m\}, \{\gamma_m\}$ can be determined and the quasi-bound state can be constructed from Eqs. (8),(9).

At this level of description a complex root search of this determinantal equation is needed in order to actually find the solutions of interest, which does not appear to make the method more efficient than various other brute force methods one might employ, such as point matching on the boundary. However there are two reasons the current method is much more powerful. First, as has been known for some time, the eigenvectors of \mathcal{S} don't change much over a range of k corresponding to the mode spacing; hence the "unquantized" solutions have the same physical content as the true quasi-bound solutions. Therefore basic physical properties such as directional emission patterns and distributions of Q-values can be obtained without the root search. Second, quite recently it was shown^{18,20} that there exists an efficient extrapolation method to find the roots once the eigenvalues of \mathcal{S} are found at two values of k , so that no true root search is necessary. The technical details supporting and expanding on these statements can be found in Ref. 18.

Once we have obtained numerical solutions to the resonance problem we would like to interpret their "classical" (ray dynamical) meaning and use our knowledge of the phase space structure and flow to explain the properties of the resonance spectrum, such as the directional emission patterns and distribution of Q-values. Despite the fact that there exists no simple classical construction of individual solutions, the correspondence between solutions and properties of the ray phase space is quite helpful in extracting the physical properties we are interested as we shall demonstrate below. The technique for extracting ray dynamical information from a real-space solution is

known as *Husimi projection*;^{18,27} this technique allows us to represent a solution within the ray phase space of the problem and ultimately on the surface of section. Such a representation attempts to extract both momentum and position information simultaneously and just as for a quantum mechanics, we cannot have full information about real-space and momentum space at the same time due to the analog of the uncertainty principle for the electromagnetic wave equation (often written as $\Delta x \Delta k \geq 1$, this is a basic property of Fourier transforms). Phase space coordinates involve both position and momentum and our resolution in phase space will be limited by this uncertainty relation.

The specific procedure which is widely followed to project a real-space

solution into phase space is a version of a “windowed” Fourier transform known as Husimi projection which involves integrating the real-space solution $\psi(\mathbf{x})$ against windowing functions peaked around position $\bar{\mathbf{x}}$

$$Z_{\bar{\mathbf{x}}\bar{\mathbf{p}}}(\mathbf{x}) = \left(\frac{1}{\pi\eta^2}\right)^{1/4} \exp(ik\bar{\mathbf{p}} \cdot \mathbf{x}) \exp\left(-\frac{1}{2\eta^2}|\mathbf{x} - \bar{\mathbf{x}}|^2\right) \quad (11)$$

where the width parameter $\eta = \sigma_0/\sqrt{k}$, σ_0 is a dimensionless parameter which can be chosen for convenience, and we note that the momentum vector has been factorized as $k\bar{\mathbf{p}}$ so that $\bar{\mathbf{p}}$ is a unit vector denoting the direction of the wavevector. The Fourier transform of this windowing function will also be a Gaussian in the unit vector \mathbf{p} peaked around $\bar{\mathbf{p}}$. In these scaled variables, which are the appropriate choice for projecting onto the billiard SOS, the uncertainty relation takes the form:

$$\Delta x \cdot \Delta p \geq \frac{1}{2k}. \quad (12)$$

The function $Z_{\bar{\mathbf{x}}\bar{\mathbf{p}}}(\mathbf{x})$ and its Fourier transform $\tilde{Z}_{\bar{\mathbf{x}}\bar{\mathbf{p}}}(\mathbf{p})$ have standard deviations which satisfy,

$$\Delta x = \frac{\sigma_0}{\sqrt{2k}} = \frac{\eta}{\sqrt{2}} \quad \Delta p = \frac{1}{\sqrt{2k}\sigma_0}, \quad (13)$$

hence they saturate this inequality and represent a “minimum uncertainty” basis for projecting the solutions onto phase space (these function are the “coherent states” often used in quantum mechanics). The Husimi density in phase space is then defined as:

$$\rho_\psi(\bar{\mathbf{x}}, \bar{\mathbf{p}}) = \left| \int d^2\mathbf{x} Z_{\bar{\mathbf{x}}\bar{\mathbf{p}}}^*(\mathbf{x}) \psi(\mathbf{x}) \right|^2, \quad (14)$$

which is positive semi-definite on the phase space of the problem. Since we have scaled $\bar{\mathbf{p}}$ to be a unit vector this phase space is already confined to the three-dimensional constant energy surface of the four-dimensional phase space, but we now wish to project it down one dimension further onto the surface of section. For this purpose it is useful to introduce windowing functions in cylindrical coordinates¹⁸ and calculate the Husimi distribution at a fixed radius $r = R_c$. Careful limiting procedures must be observed to get a meaningful result as described in Ref. 18. The resulting Husimi-SOS distribution at $r = R_c$ is given by:

$$H_\psi(\bar{\phi}, \sin \bar{\chi}) = \left| \sum_{-\infty}^{\infty} \alpha_m H_m^+(nkR_c) e^{-inkR_c(\sin \chi - \sin \bar{\chi})} \bar{\phi} e^{-\sigma_0^2(nkR_c)^2(\sin \chi - \sin \bar{\chi})^2/2} \right|^2 \quad (15)$$

where equal spatial and momentum resolution in the SOS is achieved by choosing $\sigma_0 \sim 1/\sqrt{nkR_c}$. Note that the numerical real-space wavefunction enters this expression through the coefficients α_m which are assumed known.

Equation (15) is a perfectly good Husimi-SOS distribution, but it doesn't correspond to our conventional choice of the SOS at the boundary. However, for each value of $(\bar{\phi}, \sin \bar{\chi})$ we can simply calculate the values of $(\phi, \sin \chi)$ that would result from following this ray to the boundary and assign the corresponding point on the boundary the values of the circle Husimi-SOS at $(\bar{\phi}, \sin \bar{\chi})$ corrected by a Jacobian factor for the Gaussian propagation between the two sections. This is the quantity we use to compare and interpret wave solutions in the classical SOS of the problem. Again, a detailed recipe for constructing these Husimi distributions is given in Ref. 18. Note that for the Husimi-SOS the uncertainty relation (12)

$$\Delta\phi \cdot \Delta \sin \chi \geq \frac{1}{2nkR}. \quad (16)$$

is saturated at its lower bound, i.e. $\Delta\phi \sim \Delta \sin \chi \sim 1/\sqrt{2nkR}$, where R is the average radius of the billiard and we have used the approximation that the arc length along the boundary is $R\Delta\phi$. Hence EM wave solutions only resolve the classical structures in the SOS on a scale of area $(2nkR)^{-1}$; this is the EM analog of the statement in quantum chaos theory that wavefunctions only are sensitive to classical structures of order $1/\hbar$.

To illustrate how the ray-wave correspondence works for billiards in the mixed regime we present three examples of numerical solutions for resonance wavefunctions of the quadrupole billiard calculated by the S-matrix approach and their corresponding Husimi-SOS transforms. In Fig. 7(a,b) we show a whispering gallery mode of a slightly deformed quadrupole billiard ($\epsilon = 0.03$); this is a typical wavefunction corresponding to quasi-periodic ray motion which could be calculated analytically (in principle) using the eikonal method. Projection of the state onto the SOS shows it follows closely an invariant curve of the problem, but smeared out to agree with the uncertainty relation just noted. In Fig. 7(c,d) we show a two-bounce stable orbit mode of the type one could calculate using the Gaussian optical method. In the Husimi it is well-localized on the stable island and is relatively insensitive to the existence of chaos elsewhere in the system. Thus these quite conventional modes can coexist with chaotic modes at the same deformation, as we will discuss further in Section (5.1). In Fig. 7(e,f) we show a highly chaotic mode of the strongly deformed quadrupole ($\epsilon = 0.18$). Note the "tangled" wavefronts in much of the resonator which vary in direction

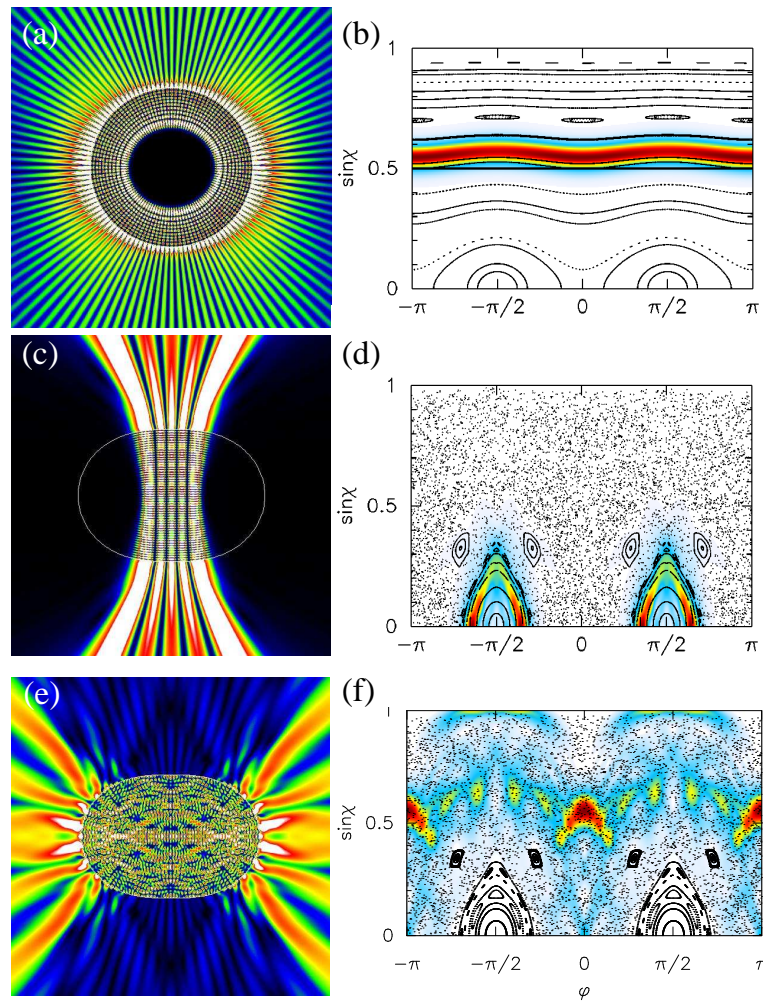


Fig. 7. Real-space false color plots and Husimi projections of (a,b) a deformed whispering gallery mode at $\epsilon = 0.03$ and $n = 2$, (c,d) transverse excited bouncing ball mode at $\epsilon = 0.16$ and $n = 2$, (e,f) mode localized on the chaotic portion of the phase space at $\epsilon = 0.18$ and $n = 2.65$.

on the scale of the wavelength. The Husimi projection shows this mode lives completely in the chaotic portion of the SOS, although it is not completely spread out on the chaotic component. From experience we find that “chaotic” solutions are still not fully randomized on the chaotic compo-

ment at the values of $nkR \sim 100 - 300$ which we can treat by our numerical method. Nonetheless the ray-wave correspondence is clearly present in these chaotic resonators and we will use it as the primary tool for interpreting the exciting experiments which have been done on ARC and spiral microlasers.

3. Ray dynamics and shape-dependent directional emission from ARCs

In the previous sections we have reviewed the phase space formulation of ray dynamics in ARCs and the formulation of the resonant scattering problem. In the current section we will begin to present the most recent experimental and theoretical developments relating to ARC resonators and lasers. First, we will review some of the experimental techniques used in the studies we report. Then we will briefly review the ray model for the directional emission of ARCs and present experimental data from two different sets of experiments on low-index ARC resonators. The first of these studied lasing emission from differently-shaped polymer ARC cylindrical microlasers¹² and the second of these studied resonant scattering from passive ARC silica microspherical cavities.²⁸ The first part of this section focuses on the lasing experiments and how they can be understood in terms of the phase space ray-dynamical method for ARCs.

3.1. *The imaging technique for the study of microcavity resonators*

The detection part of the experiment was designed in accordance with the information contained in the SOS diagram. The detector must be able to extract two pieces of information: 1) where along the sidewalls the light is emerging from the microcavity, that is, the angle ϕ , and 2) what the angle of the emitted ray is which is related to the internal incident angle χ by Snell's law of refraction. A detector that can only measure the farfield radiation pattern is insufficient because it misses where the light emerges along the sidewall. The farfield pattern alone is not unique in that the same pattern can occur for different sidewall distributions of emission. Any detection system ought to be able to distinguish between the two different emission types shown in Fig. 8, where the farfield patterns are similar, but the image patterns along the sidewalls are different.

Figure 9 shows the detection system that was settled upon as the best compromise between obtaining the farfield pattern while maintaining spa-

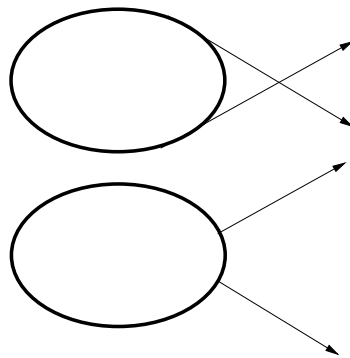


Fig. 8. Two possible emission patterns with different emitting points on the boundary, which yet can result in identical farfield distributions.

tial resolution along the sidewalls. In this setup, microlaser devices are optically pumped normal to the plane of the pillar and light emitted from the side-walls is collected through an aperture in the farfield, passed through a lens and collected on a CCD camera. The key element in this detection system is the aperture placed before the collection lens. The aperture accomplishes two purposes: 1) it limits the solid angle of the collected light; and 2) it extends the depth of field that the light is collected from. The aperture sets a solid-angle limitation and restricts the farfield profile to an angular resolution of 5 degrees. The small aperture extends the depth of field to be larger than the longest diameter of the microstructure. The depth of field associated with the numerical aperture ($NA = 0.047$) is $200 \mu\text{m}$. The largest microcavity being imaged has the longest dimension of $120 \mu\text{m}$. Thus the entire microcavity is in focus at the same time, regardless of the rotational alignment of the microcavity with respect to the camera.

The relative angle between the CCD camera and the major axis of the quadrupolar shaped microcavity is designated as θ . The relative angle is accurate to plus or minus 5 degrees and is determined by making laser-emission measurements from a square-shaped microcavity, specifically designed on the photographic mask to serve the purpose of alignment. All the other microstructures, during the mask designing time, are aligned relative to the square. The square, acting as a calibration marker, emits laser radiation (8 beams) only at its four corners and propagates parallel to its edges. Therefore, when the CCD camera is normal to one edge of the square, two equally bright spots should appear from the two edges. The relative angle is varied by either rotating the sample while keeping the CCD camera

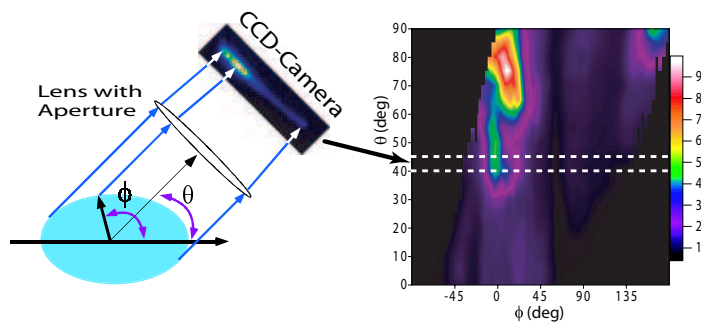


Fig. 9. Experimental setup for measuring simultaneously farfield intensity patterns and images of the sidewall emission.

stationary or vice versa.

At any given camera angle, the horizontal axis corresponds to different locations along the sidewalls. That horizontal strip gives false color coded intensity information as a function of pixels on the CCD camera, which can be converted to a position ϕ on the resonator boundary. The next angle forms another strip which is placed directly under the former strip. Measurement of the intensity is made every 5 degrees from 0 to 360. This yields a two-dimensional plot, called the *imagefield*, where a given data point $I(\phi, \theta)$ denotes the intensity emitted from sidewall position ϕ towards the farfield angle θ . The latter can easily be converted to an incidence angle $\sin \chi$, using Snell's law and basic trigonometry. Hence, what is recorded is actually a phase space plot of the emitted radiation. This correspondence is put into a rigorous basis in Ref. 18. Such 2D imagefield plots will be presented throughout the text for many of the experiments.

The farfield intensity at any angle is obtained by summing up all the pixels within the horizontal strip. This sum at a given angle is called the farfield intensity at that camera angle; we show many such plots below. This way of obtaining the farfield intensity is subtly different from placing a photomultiplier (with a pin hole) to define the angular resolution. Similarly, the *boundary image field* is obtained by integrating over all farfield angles for a fixed point ϕ on the boundary. This allows us to identify the brightest emission points on the sidewall (we rarely show these plots below, but they are used in our interpretation of the data).

A few comments are in order here. The aperture has an important role of defining a window in the direction space ($\Delta \sin \chi$), so that a given pixel on the camera can be identified upto a diffraction limited resolution with a

pair $(\phi, \sin \chi)$. Mathematically, the effect of the lens-aperture combination is equivalent to a windowed Fourier transform of the incident field on the lens.²⁹ Note that infinite aperture limit is simply a Fourier transform of the incident field and we lose all the information about direction $\sin \chi$, consistent with our intuition with conjugate variables. It has to be emphasized that we are only probing the farfield, and hence the image-data does not contain the “nearfield” details we would see in a typical numerical solution, nor does it contain information about the internally reflected components of the internal cavity field (see Ref. 20 for further details). On the other hand, it provides us with valuable information as to the $\sin \chi$ - ϕ correlations in the emitted field, allowing us to put forward a ray interpretation of the emission and hence the internal resonance.

3.2. Phase space ray escape model for emission from ARCs

In Section (2.3) we discussed the ray dynamics of ARCs using the surface of section to illustrate the generic properties of mixed phase space and contrast them with integrable dynamics. In that section the ARC was treated as a closed two-dimensional billiard with specular reflection and zero loss. We saw that the ray dynamics is qualitatively different for an integrable billiard shape, such as the circle or ellipse, as compared to a generic, partially-chaotic billiard shape such as the quadrupole. An implication of that difference (illustrated in Fig. 14 below) is that for the ellipse, which is integrable for any eccentricity, phase space flow occurs on a one-dimensional curve in the SOS and the variations in angle of incidence $\sin \chi$ are bounded for any initial condition. For generic shapes there are regions of phase space corresponding to chaotic motion for which motion in the SOS fills a two-dimensional region in a diffusive manner, and for deformations above 10% these chaotic regions typically make up a large fraction of the phase space. A dielectric cavity differs from an ideal metallic cavity in that rays at angles of incidence below the critical angle $\sin \chi_c = 1/n$ are partially refracted out of the cavity providing a new mechanism for emission into the farfield which differs from the evanescent coupling of whispering gallery modes. In a series of papers beginning in 1994, Nöckel, Stone and Chang^{4,5,30,31} proposed to model the resonant emission from ARCs by a ray escape model in which an initial bundle of rays was propagated in phase space and allowed to escape the ARC according to a physically-motivated “escape rule”; the mean rate of escape and the distribution in angle of the outgoing rays were used to predict the Q-values and emission patterns

from ARCs. The escape rule reduces to the Fresnel law of refraction from a flat interface for angles of incidence below the critical angle but takes into account the tunneling (evanescent) leakage which occurs for a curved interface when the angle of incidence is above the critical angle for total internal reflection. It should be pointed out that these tunneling corrections are unimportant when the ray dynamics is highly chaotic and the critical angle is rapidly crossed, but become crucial for small perturbations where initial rays remain above the critical angle (this situation will be relevant to the silica ARC experiments reported below).

A challenging point for the general definition of such a model is that in the case of chaotic dynamics there is no simple correspondence between a set of rays and a set of modes of the wave equation (as there is in the integrable case – see Section (2.2)). Nöckel and Stone proposed^{5,31} that an appropriate set of initial conditions for ARCs would be to start a uniform distribution of rays on an adiabatic curve of the boundary,^{23,32} which can be thought of as the curve in the SOS that a ray *would* follow in the absence of chaos (this approximation describes the exact flow in the ellipse, see Fig. (10) for an example). Using this model they were able to predict a striking difference in the emission patterns from quadrupole resonators with index $n = 1.5$ as opposed to index $n = 2.0$. They also noted that this difference was not highly sensitive to the choice of initial conditions. The theoretical analysis we present here indicates that the adiabatic model does not apply over most of the experimental range but that the ray escape model still gives good results, because its predictions for high deformations are almost completely independent of initial conditions for ARCs with index of refraction $n \approx 1.5$. The ray model and its independence of initial conditions for a strongly deformed quadrupole ARC is illustrated in Fig. 10.

3.3. Tests of the ray model in polymer ARC lasers

Note that the emission pattern for the quadrupole at $\epsilon = 0.12$ and index $n = 1.5$ is predicted by the ray model to be highly directional with a peak in roughly the 35° direction in the farfield. Below we will see that this emission directionality for this shape is observed experimentally and also is found in numerical solutions of the wave equation. As pointed out in the initial work,^{30,5,31} this emission pattern contradicts the intuitive expectation that the resonator should emit from the points of highest curvature ($\phi = 0, \pi$) in the tangent direction (critical emission) which would lead to peaks at $\theta = \pm\pi/2$ in the farfield. Moreover in later work³³ it was shown that an

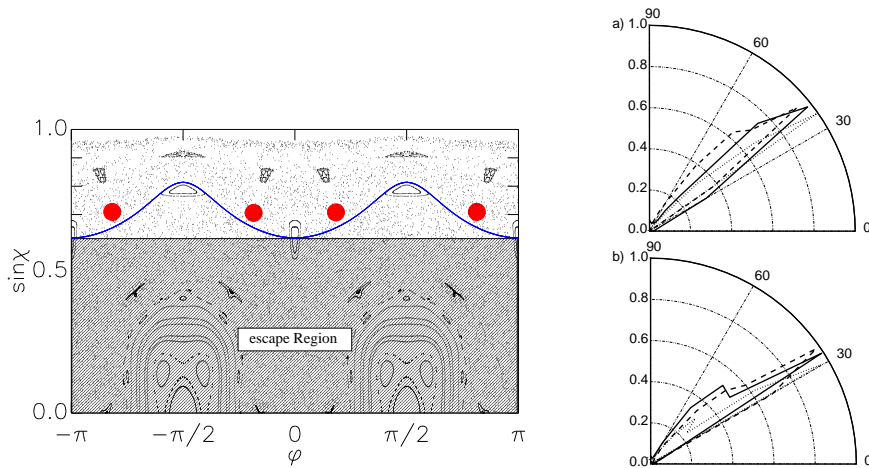


Fig. 10. left: Surface of section of the quadrupole ARC with $\epsilon = 0.12$ and index of refraction $n = 1.5$. The portion of the SOS below $\sin \chi_c = 1/n$ is shaded to indicate that in this region rays escape rapidly by refraction. In color we have indicated two possible types of initial conditions used in the ray escape model; the blue curve represents one of the possible adiabatic curves which were used as initial conditions in the Nöckel-Stone model and the red circles initial conditions localized on the unstable 4-bounce orbit. A third initial condition used extensively below is simply to start randomly on all possible points in the SOS originating in the trapped region above the critical line. Right: farfield emission plots calculated using the ray escape model for this system with the three possible choices of initial conditions just described. The qualitative and semi-quantitative features of the emission patterns are seen to be independent of the choice of initial conditions for this system. right: Ray simulations of the farfield emission patterns for the quadrupole with $\epsilon = 0.12$ (a), $\epsilon = 0.18$ (b) with different types of initial conditions. The solid curve is the result of choosing random initial conditions about the critical line $\sin \chi = 1/n$, the dashed curve is for initial conditions on the adiabatic curve with minimum value at the critical line. The dotted curve is for initial conditions localized around the unstable fixed point of the rectangle periodic orbit. In each of the ray simulations 6000 rays were started with unit amplitude and the amplitude was reduced according to Fresnel's law upon each reflection, with the refracted amplitude "collected" in the farfield. The emission pattern found by the ray model agrees well with microlaser experiments.

ellipse with the same index of refraction and the same major to minor axis ratio emits in the $\pm\pi/2$ direction as intuitively expected. This suggested a very dramatic shape sensitivity of the emission patterns, as the ellipse and the quadrupole are identical shapes to leading order in ϵ . In that same work³³ experiments on deformed spherical lasing droplets were interpreted in terms of the ray model for the quadrupole ARC (Fig. 10). While suggestive, those experiments did not have the ability to study a specific defined

shape and were complicated by the three-dimensional nature of the modes of the droplet. Here we focus on experiments on polymer microcylinder lasers which do not suffer from these drawbacks.

In the polymer lasing experiments deformed cylindrical lasers were fabricated with shapes defined by a mask to approximate closely shapes which would exhibit these different behaviors. In the specific experiments we now discuss the shapes studied were cylinders with elliptical, quadrupolar and hexadecapolar deformations of between ten and twenty percent¹² (see precise definitions, caption of Fig. 11). As noted, the ellipse for any eccentricity gives integrable ray dynamics and the quadrupole and hexadecapole are two simple examples of generic shapes with mixed dynamics. We will see that the boundary shape of the microlaser does indeed have a dramatic influence on the emission patterns. Here we will only discuss in detail the comparison of the ellipse and the quadrupole; a more detailed study including the quadrupole-hexadecapole shaped ARCs is reported in Schwefel *et al.*¹²

As already noted, earlier work³³ had predicted that quadruple ARCs with index $n = 1.5$ and deformation in the range of 10-12% would emit primarily in the $\theta = 35^\circ - 45^\circ$ direction in the farfield while an ellipse with the same major-minor axis ratio emits primarily in the $\theta = 90^\circ$ direction (as one might have expected). It was argued that the origin of this effect is the presence in the quadrupole of a stable four-bounce periodic ray orbit which prevents emission from the highest curvature points in the tangent direction, an effect termed “dynamical eclipsing”.^{30,31} This finding was supported by numerical solutions of the linear wave equation for the quasi-bound states and their farfield emission patterns. Mode selection and non-linear lasing processes were not treated in the theory. This earlier work on ARCs did not look extensively at deformations above $\varepsilon = 0.12$ for the case of low index materials such as polymers or glass. The belief was that the adiabatic model would become questionable at higher deformations as the phase space became more chaotic and the ray motion departed from the adiabatic curves very rapidly. A natural expectation was that due to increased chaos the emission patterns in the farfield would become less directional and more fluctuating. The experimental data we now review¹² strongly contradicts this expectation.

3.4. *Experimental results*

The experiments we report were performed by Rex *et al.*^{10,12} on differently shaped dye (DCM)-doped polymer (PMMA) samples that are fabricated

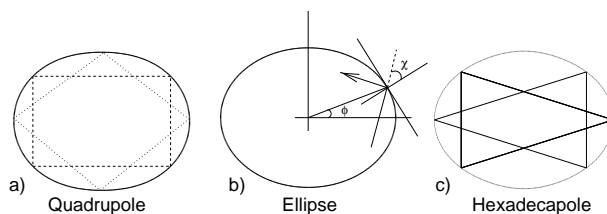


Fig. 11. Cross-sectional shapes of micropillar resonators studied: a) The quadrupole, defined in polar coordinates by $R = R_0(1 + \varepsilon \cos 2\phi)$, b) The ellipse, defined by $R = R_0(1 + ((1 + \varepsilon)^4 - 1) \sin^2 \phi)^{-1/2}$ and c) The Quadrupole-Hexadecapole, defined by $R = R_0(1 + \varepsilon(\cos^2 \phi + \frac{3}{2} \cos^4 \phi))$ all at a deformation of $\varepsilon = 0.12$. Note that all shapes have horizontal and vertical reflection symmetry and have been defined so that the same value of ε corresponds to approximately the same major to minor axis ratio. In a) we show short periodic orbits (“diamond, rectangle”) relevant to the discussion below.

on top of a spin-on-glass buffer layer coated over a silicon substrate via a sequence of micro-lithography and O_2 reactive ionic etching steps. The effective index of refraction of these microcavities is 1.49, much lower than for other experiments (discussed below) which were performed using a similar set-up on GaN, where the index of refraction is $n = 2.65$.^{34,11} The cavities are optically pumped by a Q-switched Nd:YAG laser at $\lambda = 532$ nm incident normal to the plane of the micropillar. Light emitted from the laser is imaged through an aperture subtending a 5° angle and lens onto a ICCD camera which is rotated by an angle θ in the farfield from the major axis. A bandpass filter restricts the imaged light to the stimulated emission region of the spectrum. The ICCD camera records an image of the intensity profile on the sidewall of the pillar as viewed from the angle ϕ which is converted from pixels to angular position ϕ . Here we show microcavities with elliptic and quadrupolar shape of an average radius $R_0 = 100\mu\text{m}$ (see formulas in Fig. 11 caption). Each shape was analyzed at eccentricities of $\varepsilon = 0.12, 0.14, 0.16, 0.18$ and 0.20 .

In Fig. 12 we show the experimental results in the form of a color scale 2D imagefield (ϕ, θ) plot as discussed previously. We omit the data for $\varepsilon = 0.14$ deformation as it indicates no effects not captured by the data at the other deformations. As insets we show the exact shape of each of the microcavities. Although the shapes appear very similar to the eye, we find dramatic differences in the farfield emission patterns, which in the case of the ellipse vs. the quadrupole, persist over a wide range of deformations. Specifically, the farfield emission intensity for the quadrupole exhibits a strong peak at $\theta = 34^\circ - 40^\circ$ which remains rather narrow over the observed

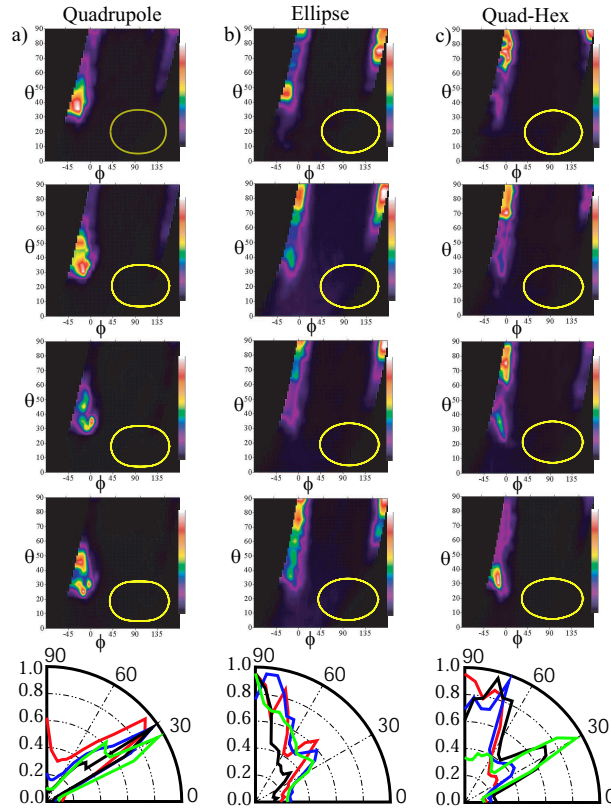


Fig. 12. Two-dimensional display of the experimental data showing in false color scale the emission intensity as a function of sidewall angle ϕ (converted from ICCD images) and of the farfield angle θ (camera angle). Columns from left to right represent the quadrupole, ellipse and quadrupole-hexadecapole respectively. Insets show the cross-sectional shapes of the pillars in each case (for definitions see Fig. 11). The graphs at the bottom show the farfield patterns obtained by integration over ϕ for each θ , normalized to unity in the direction of maximal intensity. The deformations are $\varepsilon = 0.12, 0.16, 0.18, 0.20$ (red, blue, black and green respectively)

range of deformations. Over the same range of deformation the boundary image field (not shown) for the quadrupole changes substantially and does not exhibit one localized point of emission. In contrast, the ellipse emits into the $\theta \sim 90^\circ$ direction in the farfield, but with a much broader angular intensity distribution, while the boundary image field remains well-localized around $\phi \sim 0^\circ$ (the point of highest curvature in the imaged field). Thus we see qualitatively different behaviors for the two shapes studied over the

same range of variation of the major to minor axis ratios. The hexadecapole shape shows yet a third behavior with a cross-over between ellipse-like and quadrupole-like patterns with increasing deformation; the origin of this is discussed in Ref. 12; this shape will not be analyzed further here.

Several different samples with the same boundary shape were measured in each case and confirmed that the basic features of this data set are reproduced within each class (with small fluctuations).¹⁰ This shows that the effects measured are a property of the boundary shape and not of uncontrollable aspects of the fabrication process. Moreover the theoretical calculations, which we will present next, are based on uniform dielectric rods with the ideal cross-sectional shape specified by the mask; therefore the agreement of these calculations with the measurements also confirms that the differences are due to controllable shape differences.

3.5. Ray and wave simulations of polymer experiments

The experiment is performed well into the short-wavelength limit, and we employ the ray escape model of Nöckel and Stone described above (caption, Fig. 10) to calculate the emission patterns. To compare with experiment we collected the emitted rays in 5° bins. As shown above (Fig. 10), for the quadrupole the basic results are independent of initial conditions over a wide range and we employ a uniform random set of ray initial conditions above the critical line for escape. In the case of the non-chaotic ellipse the results are not independent of initial conditions and we chose initial conditions localized on invariant curves near the critical angle (this improves agreement with experiment and is more physically reasonable).

In addition to these ray simulations we also performed exact numerical calculations of the resonances of the passive cavity using the S-matrix method described in Ref. 35 and reviewed in Section (2.4). This method generates the entire range of high-Q and low-Q resonances for such a cavity and thus there is some arbitrariness in choosing which resonance to compare with the experiment. Previous experiments have indicated that mode selection is complicated in these dielectric resonators and that there is no simple rule relating the observed lasing mode to the Q-value of the mode in the passive cavity. Due to their low output coupling and the multi-mode nature of these lasers, high Q-modes are not necessarily the observed lasing modes in the farfield. This set of experiments did not allow the collection of spectral data and the Q-values of the lasing modes are not directly measured. Thus from the set of calculated resonances we chose the resonance

which coincides well with the observed farfield pattern and has a relatively high $Q = -2\text{Re}[k]/\text{Im}[k]$. We also confirmed that theoretical 2D imagefield data coincides well with the experimental results. Moreover in all cases discussed here, there were many resonances which gave good agreement with the data, indicating the existence of a robust class of modes any of which could be the lasing mode.

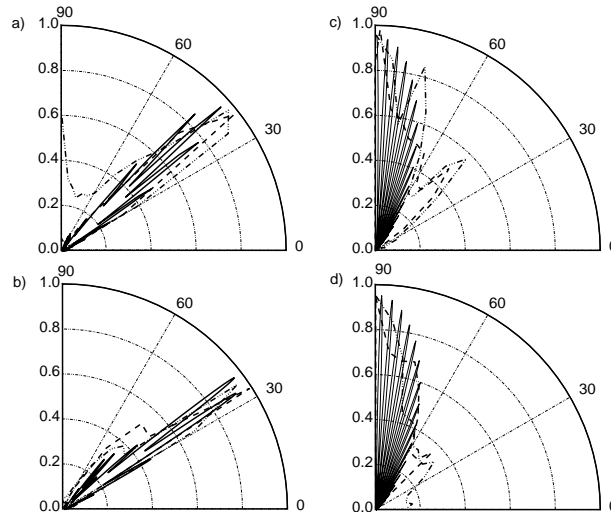


Fig. 13. Farfield intensity for the quadrupole (a, b) and ellipse (c, d) with $\varepsilon = 0.12$ (a, c) and 0.18 (b, d). The dash-dotted curve is the experimental result, dashed the ray simulation and solid a numerical solution of the wave equation. The ray simulation for the quadrupole was performed starting with 6000 random initial conditions above the critical line and then propagated into the farfield in the manner described in the text. The ray simulation for the ellipse was performed starting with 6000 initial conditions spread over seven caustics separated by $\Delta \sin \chi = 0.02$ below the critical caustic (the caustic that just touches the critical line). The numerical solutions selected for the quadrupole have $kR_0 = 49.0847 - 0.0379i$ with a $Q = -2\text{Re}[kR_0]/\text{Im}[kR_0] = 2593.05$ and $kR_0 = 49.5927 - 0.0679i$ with $Q = -2\text{Re}[kR_0]/\text{Im}[kR_0] = 1460.72$ for $\varepsilon = 0.12$ and 0.18 respectively. The numerical wave solutions for the ellipse shown correspond to $kR_0 = 49.1787 - 0.0028i$ with $Q = -2\text{Re}[kR_0]/\text{Im}[kR_0] = 17481.38$ and $kR_0 = 49.2491 - 0.0110i$ with $Q = -2\text{Re}[kR_0]/\text{Im}[kR_0] = 4488.20$ for $\varepsilon = 0.12$ and 0.18 respectively.

In Fig. 13 we compare the experimental results for the farfield emission patterns for the two shapes measured at $\varepsilon = 0.12, 0.18$ to both the ray model and the wave calculations. The agreement in both cases is quite good. In Fig. 13 we show in red the numerical farfield by calculating the asymptotic expansion of our wavefunction in the farfield. Numerical limitations prevent

us from performing the calculations at the experimental values of $kR_0 \sim 1000$ but the major features of the emission pattern are not sensitive to kR_0 over the range we can study numerically. The finding (discussed next) that we can reproduce these patterns from ray escape simulations also suggests that the wavelength is not a relevant parameter for the features we are studying. In green we show the experimental results.

4. Surprising features of the data

The strong sensitivity of the emission patterns to small differences in boundary shape is quite striking. This sensitivity was predicted in the earlier work of Refs. 30, 31, 33 and was therefore not unexpected. However there are major aspects of the experimental data which *are* quite surprising even in the light of the earlier work on ARCs. In particular, the persistence of highly directional emission in the quadrupolar shapes at quite high deformations was not predicted theoretically and was unexpected for reasons we will now discuss. In order to understand the unexpected features of the data and to develop principles to predict the emission patterns for untested boundary shapes we now present recent theoretical arguments about phase space flow in these systems which can account for the persistence of directional emission to high deformations and high degree of chaos.

4.1. Dynamical eclipsing effect

We begin by briefly reviewing the adiabatic picture used previously to discuss the directional emission from the quadrupole. In Section (2.3) we reviewed the concept of phase space flow and the Poincaré surface of section. In Fig. 14 we exhibit the difference in phase space structure between the ellipse and the quadrupole. While the behavior of the quadrupole shown in Fig. 14A) is generic there do exist special billiards that exhibit the two extremes of dynamical behavior. One limiting case already noted is the integrable billiard exemplified by the ellipse billiard, the SOS of which is shown in Fig. 14B). Due to its integrability, phase space flow in the ellipse is particularly simple: every initial condition lies on one of the invariant curves given by Eq. (17) below, and the trajectory retraces this curve indefinitely (see Fig. 14B)). Curves which cross the entire SOS correspond to real-space motion tangent to a confocal elliptical caustic Fig. 14B)(a); curves which do not cross the entire SOS represent motion tangent to a hyperbolic caustic in real space Fig. 14B)(b). The ellipse was conjectured to be the only convex deformation of a circular billiard which is integrable,³⁶ and a recent

proof of this was given by Amiran.³⁷ At the opposite extreme is the Bunimovich stadium billiard (see inset in Fig. 19) for which it is proven that there exist no stable periodic orbits and the entire phase space (except sets of measure zero) is chaotic. We will study theoretically the emission from stadium-shaped resonators in Section (4.4).

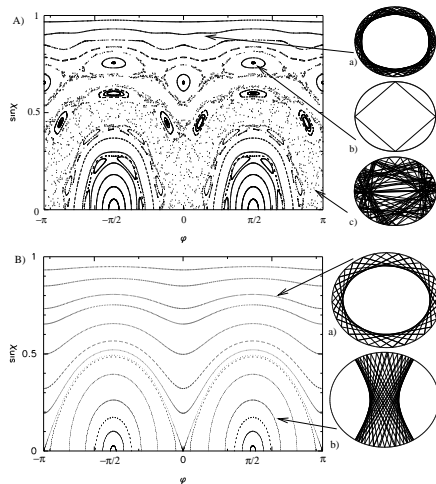


Fig. 14. The Poincaré surface of section for the quadrupole A) and the ellipse B) with $\varepsilon = 0.072$. The schematics A)(a-c) on right show three classes of orbits for the quadrupole, A)(a) a quasi-periodic orbit on a KAM curve, A)(b) a stable period-four orbit, (the ‘diamond’), and A)(c) a chaotic orbit. Schematic B)(a, b) show the two types of orbits which exist in the ellipse, the whispering gallery type, with an elliptical caustic B)(a) and B)(b), the bouncing ball type, with a hyperbolic caustic.

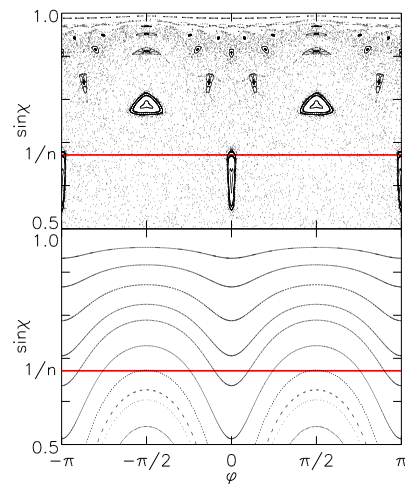


Fig. 15. Comparison of the Poincaré surface of section for the quadrupole and the ellipse with $\varepsilon = 0.12$ showing mostly chaotic behavior in the former case and completely regular motion in the latter. The red line denotes $\sin \chi_c = 1/n$, the critical value for total internal reflection; rays above that line are trapped and those below escape rapidly by refraction. The quadrupole still exhibits stable islands at $\phi = 0, \pi$ and $\sin \chi = \sin \chi_c$ which prevent escape at the points of highest curvature in the tangent direction

Phase space flow in mixed systems is much more complex and is ergodic on each chaotic region. However a key property of mixed dynamical systems is that the different dynamical structures in phase space are disjoint; this implies that in two dimensions KAM curves and islands divide phase space into regions which cannot be connected by the chaotic orbits. This puts constraints on phase space flow despite the existence of chaos in a significant fraction of the phase space. For small deformations ($\sim 5\%$) most of phase

space is covered by KAM curves the form of which can be estimated using an adiabatic approximation.³¹ This approximation gives the exact result for all deformations in the case of the ellipse; it can be written in the following form:

$$\sin \chi(\phi) = \sqrt{1 + (S^2 - 1)\kappa^{2/3}(\phi, \varepsilon)} \quad (17)$$

where κ is the radius of curvature along the boundary and S is a constant. Plotting this equation for different values of S, ε gives an SOS of the type shown in Fig. 14B). For the mixed case, exemplified by the quadrupole billiard in Fig. 14A), Eq. (17) describes quite accurately the behavior for values of $\sin \chi$ near unity, but doesn't work well at lower $\sin \chi$ where chaos is more prevalent.

Nöckel and Stone used the adiabatic curve picture to give a qualitative explanation for the difference in emission patterns between the quadrupole at $n = 1.5$ and the ellipse for the same index (or the quadrupole for $n = 2.0$). The idea was that for some range of deformations the phase space flow in the quadrupole could be seen as rapid motion along adiabatic curves and slow diffusion between them. The adiabatic invariant curves for the quadrupole have their minimum values of $\sin \chi$ at the points of highest curvature on the boundary $\phi = 0, \pm\pi$, just as they do in the ellipse. If the diffusion in phase space is sufficiently slow, emission would be near these points of highest curvature and at the critical angle, i.e. in the tangent direction, as in the ellipse. This reasoning held as long as the escape points $\sin \chi = 1/n, \phi = 0, \pm\pi$ occurred in the chaotic region and were reachable from the totally-internally-reflected region of $\sin \chi > 1/n$. This is the calculated behavior for $n = 2$ quadrupole.³¹ However for $n = 1.5$ quadrupole and deformations around 10%, these expected emission points are enclosed by the stable island corresponding to the four-bounce "diamond" orbit and due to the disjoint nature of the dynamics, "chaotic" rays cannot escape there. Instead they will escape at higher or lower values of ϕ leading to a large change in the emission pattern from that of the ellipse with similar minor-major axis ratio. This phenomenon was termed "dynamical eclipsing".

Figure 15 contrasts the phase space for the ellipse and the quadrupole for $\varepsilon = 0.12$. The island associated with the stable diamond orbit is smaller than at $\varepsilon = 0.072$, but is still present for the quadrupole; there is no such island at any deformation for the ellipse. Note that in the experimental data for the quadrupole at $\varepsilon = 0.12$ we do not see a bright spot at the boundary at $\phi = 0$, consistent with the dynamical eclipsing model in which the island structure forces the chaotic WG modes to emit away from the

point of highest curvature. In contrast the bright spot in the ellipse which emits to $\theta = 90^\circ$ clearly is at $\phi = 0$ for $\varepsilon = 0.12$. Thus the adiabatic model of Refs. 31, 30 does seem consistent with the data for $\varepsilon = 0.12$ in the quadrupole.

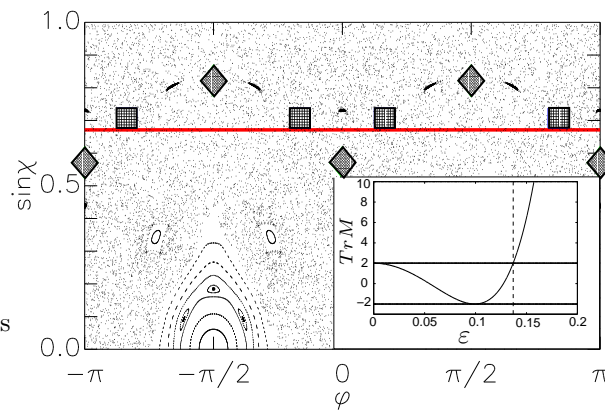


Fig. 16. Poincaré surface of section for the quadrupole with $\varepsilon = 0.18$. The grey line indicates the critical angle of incidence. The diamonds indicate the location of the fixed points of the (now) unstable “diamond” orbit and the squares the fixed points of the unstable rectangular orbit. In the inset we show the trace of the monodromy (stability) matrix (see Eq. 20) for the diamond orbit versus deformation. When the magnitude of the trace of the monodromy matrix is larger than two its eigenvalues become real, the periodic motion becomes unstable and the associated islands vanish. For the diamond this happens at $\varepsilon = 0.1369$ (see dashed vertical line in the inset) and the simple dynamical eclipsing picture of Fig. 15 does not apply at larger deformations.

4.2. Short-time dynamics and Unstable Manifolds

At higher deformations chaotic diffusion is fast and rays tend to escape rapidly even if they are initially well confined (i.e. far away from the critical angle). It is not at all clear that the motion in phase space is equivalent to slow diffusion between adiabatic curves. An iteration of random initial conditions above the critical angle for 50 steps in the closed billiard is shown in Fig. 17. It reveals a structure in the short-term dynamics which is not similar to the adiabatic curve model and actually breaks the reflection symmetry of these curves (and of the infinite time SOS) around $\phi = 0$. The colored curves which actually determine this flow pattern are the unstable manifolds of short periodic orbits in the system. We now review briefly this fundamental concept in non-linear dynamics.

4.3. Unstable Manifolds

The SOS is defined by a discrete map of the billiard dynamics. One can get a good idea of the short term dynamics of a chaotic region of such a map by linearizing it in the neighborhood of unstable fixed points (corresponding to unstable periodic orbits in real space). If we take the initial position and direction/momentum of one ray at the boundary to be $(s, u) = (\phi, \sin \chi)$ we define the map which projects the ray to the next position and direction to be

$$T : (\phi, \sin \chi) \rightarrow (\phi', \sin \chi'). \quad (18)$$

A set of fixed points of order N is defined by

$$T^N(\phi, \sin \chi) = (\phi, \sin \chi). \quad (19)$$

We can propagate an initial ray corresponding to a small deviation from the fixed point values by linearizing the map around the fixed point.

$$T(\phi, \sin \chi) \sim M(\phi, \sin \chi) = \begin{pmatrix} \frac{\partial s'(s,u)}{\partial s} & \frac{\partial u'(s,u)}{\partial s} \\ \frac{\partial s'(s,u)}{\partial u} & \frac{\partial u'(s,u)}{\partial u} \end{pmatrix} (\phi, \sin \chi)^T \quad (20)$$

The nature of the nearby motion can then be characterized by calculating the eigenvalues and eigenvectors of M . For Hamiltonian flows M is always an area-preserving map, i.e. $\det M = 1$. The matrix M is also known as the *monodromy*, or *stability* matrix. The eigenvalues can be either complex on the unit circle or purely real and reciprocal to each other. If the eigenvalues are complex, the fixed points are stable (elliptic) and nearby points oscillate around the fixed points tracing an ellipse in the SOS. In this case the long-time dynamics is determined by the linearized map to a good approximation. In the case of real eigenvalues there will be one eigenvalue with modulus larger than unity (unstable) and one with modulus less than unity (stable) and there will be two corresponding eigendirections (not usually orthogonal). In the stable direction, deviations relax exponentially towards the fixed points; in the unstable direction deviations grow exponentially away from the fixed points. Generic deviations will have at least some component along the unstable directions and will also flow out along the unstable direction. Therefore, in a short time generic deviations move out of the regime of validity of the linearized map and begin to move erratically in the chaotic “sea”. Hence the linearized map is not a good tool for predicting long time dynamics in a chaotic region of phase space. However, in open billiards, rays will escape if they wander away from the fixed points into the part of the chaotic sea which is below the critical angle

for total internal reflection. Therefore we find the unstable eigenvectors of the short periodic orbits useful in predicting ray escape. For the short periodic orbits in our shapes it is possible to calculate the matrix M giving the linearized map around all of the short periodic orbits. Thus we can calculate the eigendirections and determine the unstable directions analytically. For deviations away from the fixed points which are outside the range of validity of the linear approximation to the map one can still define generalized curves known as the stable and unstable *manifolds* of the periodic orbit which describe the set of points which would approach the fixed points asymptotically closely as $t \rightarrow \infty, t \rightarrow -\infty$ respectively. Each unstable fixed point has associated with it stable and unstable manifolds which coincide with the eigendirections as one passes through the fixed point. Note that for integrable systems there is only one asymptotic manifold for both past and future and it coincides exactly with the invariant curves, which can be calculated analytically in some cases (e.g. the ellipse). For the non-integrable case, e.g. the quadrupole, we can only calculate the eigendirections near the fixed point analytically and must trace out the full manifolds numerically. As the unstable manifolds deviate further from the fixed points, generically they begin to have larger and larger oscillations. This is necessary to preserve phase space area while at the same time have exponential growth of deviations. This tangling of the unstable manifolds has been used to devise a mathematical proof of chaotic motion.³⁸ Strikingly, we see in Fig. 17 that the phase space flow at large deformations is perfectly predicted by the shape of the unstable manifolds of the short periodic orbits in that region of phase space.

One can argue qualitatively that the unstable manifolds of the short periodic orbits ought to control the ray escape dynamics at large deformations. The manifolds of short periodic orbits are the least convoluted as they are typically the least unstable; hence the unstable direction is fairly linear over a large region in the SOS. A typical ray will only make small excursions in phase space until it approaches one of these manifolds and then it will rather rapidly flow along it. If the direction leads across the critical line for escape, that crossing point and the portion just below will be highly favored as escape points in phase space. Note further that the different unstable manifolds must fit together in a consistent manner and cannot cross one another; if they did such a crossing point would define a ray which asymptotically in the past approaches two different sets of fixed points, which is not possible. Because of this non-crossing property the unstable manifolds define just a few major flow directions in the SOS. To see

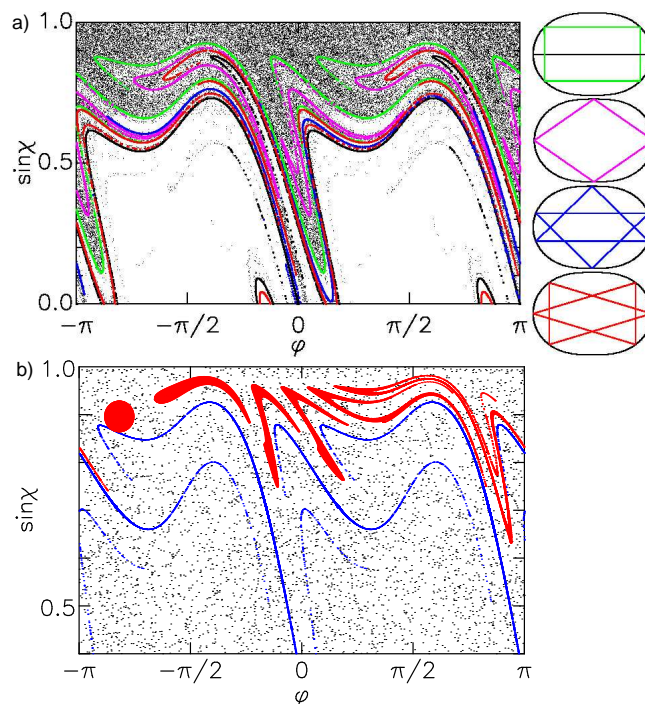


Fig. 17. (a) Ray simulations of short-term dynamics for random initial conditions above the critical line, propagated for 10 iterations, plotted on the surface of section for the quadrupole with $\varepsilon = 0.18$. The areas of the SOS covered are delineated very accurately by the unstable manifolds of the short periodic orbits which are indicated in the schematics at right. These manifolds are overlaid in the figure with appropriate color coding. (b) Flow of phase space volume in the surface of section of the quadrupole with $\varepsilon = 0.18$. A localized but arbitrary cloud of initial conditions (red) is iterated six times to illustrate the flow. The initial volume is the circle at the far left, successive iterations are increasingly stretched by the chaotic map. The stretching clearly follows closely the unstable manifold of the rectangle orbit which we have plotted in blue.

this more explicitly, in Fig. 17b) we propagate an arbitrary but localized set of initial conditions and see that they are stretched along and parallel to nearby unstable manifolds. Thus it appears that for the highly deformed case the phase space flow of a generic ray is much better predicted by simply plotting these manifolds.

As a confirmation that these manifolds do control escape we perform a further ray simulation for the “open” billiard. We propagate, as before, an ensemble of rays with a uniform random distribution above the critical angle. As we have done in calculating the ray emission pattern, we asso-

ciate to every starting ray in the surface of section an amplitude which decreases as the ray propagates forward in time according to Fresnel's law (if the point falls below the critical line). Instead of following the refracted amplitude into the farfield, in this case we plot the *emitted* amplitude onto the surface of section, as shown in Fig. 18a). The emission amplitude is almost completely confined within the two downwards "fingers" created by the unstable manifold of the four-bounce rectangular orbit. As noted earlier, the availability of the two-dimensional data obtained from the imaging technique (see Fig. 12), gives us a unique ability to reconstruct the emitting part of the lasing mode both in real space and momentum space directly from experimental data. It is therefore possible to check directly this ray simulation in phase space against experimental data. The intensity data is sorted into intensity pixels according to both its sidewall location (the angle ϕ from which emitted intensity originated) and its farfield angle, which by geometric considerations and Snell's law can be converted to the internal angle of incidence $\sin \chi$. Therefore we can project this data "back" onto the SOS for emission. In Fig. 18b) we show this projection for the same deformation as in Fig. 18a); we find remarkable agreement between the projected data and the ray simulation. As noted above, this is a much more demanding test of agreement between theory and experiment than simply reproducing the experimental farfield patterns.

Although the phase space flow along the unstable manifolds leads to a highly non-uniform emission pattern in phase space, this alone does not fully explain the very narrow farfield emission peak observed in the data. We see in Fig. (18a) that there is still a significant spread of angles of incidence for escape. In fact the spread of escape angle we see in Fig. 18 would lead to an angular spread of nearly 80° in the farfield if all the escape occurred from the same point on the boundary. However as we see from Fig. 18, the point of escape and the angle of incidence are correlated and vary together according to the shape of the unstable manifold. Because the boundary is curved, different angles of incidence can lead to the same angle of emission in the farfield. It is straightforward to calculate the curves of constant farfield for a given shape; for the quadruple at $\varepsilon = 0.18$ this curve for the peak observed emission angle of 34° is plotted in Fig. 18. The curve tends to lie remarkably close to the unstable manifold. Therefore we find that the curvature of the boundary tends to compensate almost completely for the dispersion in the angle of incidence at escape.

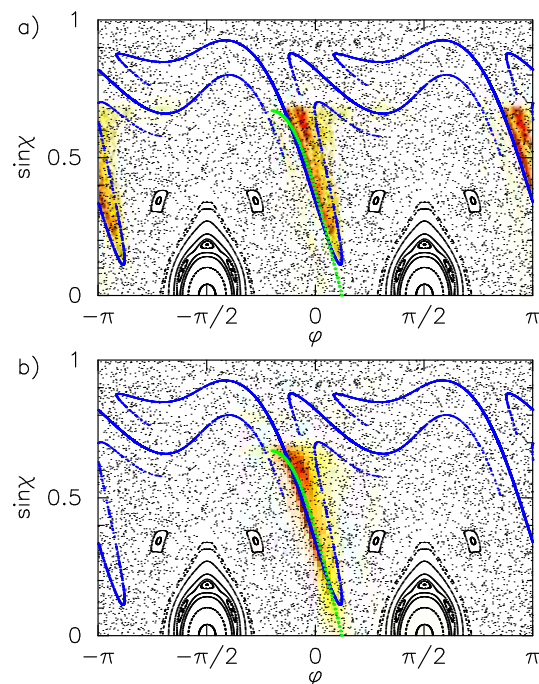


Fig. 18. a) Ray simulation of emission: emitted ray amplitude (color scale) overlaid on the surface of section for the quadrupole with $\varepsilon = 0.18$. b) Farfield intensity from experimental image data Fig. 12 projected in false color scale onto the surface of section for the quadrupole with $\varepsilon = 0.18$. The blue line is the unstable manifold of the periodic rectangle orbit. In green we have the line of constant 34° farfield (see the discussion in Section (4.3)). Absence of projected intensity near $\phi = \pm\pi$ in (b) is due to collection of experimental data only in the first quadrant.

4.4. Directional Emission from Completely Chaotic Resonators

The existence of highly directional emission for the highly deformed quadrupole ($\varepsilon = 0.20$) suggests that the slow diffusion in phase space, characteristic of mixed systems, is not essential to get this effect. Therefore we decided to study theoretically resonators for which the corresponding billiard is completely chaotic and for which there exist no stable periodic orbits at all. The Bunimovich Stadium (see inset in Fig. 19), mentioned above, was a natural choice due to its similarity to the quadrupole. As before we did both ray escape simulations and numerical solutions of the wave equation. In Fig. 19 we show our predictions. We find again highly directional

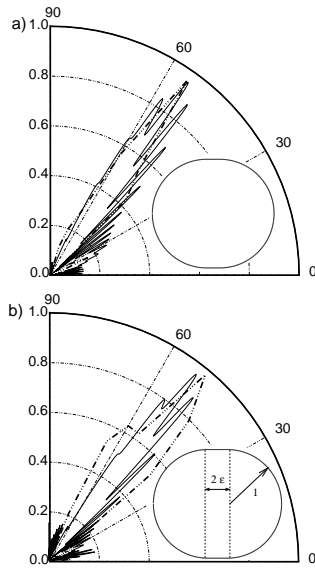


Fig. 19. Farfield emission patterns for the stadium with $\varepsilon = 0.12, 0.18$. The dash-dotted curve is the ray simulation and the solid a numerical solution of the wave equation; no experimental data was taken for this shape. The ray simulation was performed with random initial conditions exactly as in Fig. 10. The numerical solutions were for resonances with $kR = 50.5401 - 0.0431i$ with $Q = -2\text{Re}[kR]/\text{Im}[kR] = 2342.71$ and $kR = 48.7988 - 0.1192i$ with $Q = -2\text{Re}[kR]/\text{Im}[kR] = 818.83$ for $\varepsilon = 0.12$ and 0.18 respectively. The inset shows the shape of the stadium; it is defined by two half circles with radius one and a straight line segment of length 2ε .

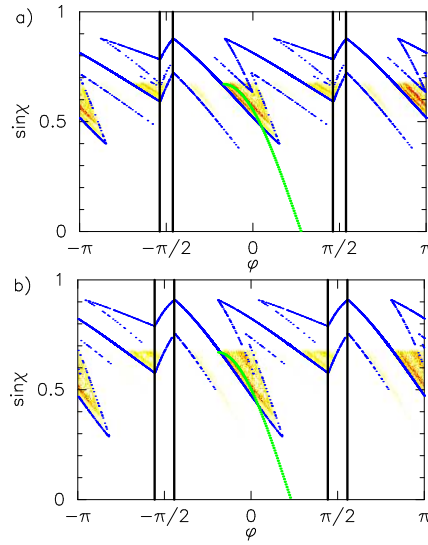


Fig. 20. Ray emission amplitude (color scale) overlaid on the surface of section for the stadium with $\varepsilon = 0.12$ (a) and $\varepsilon = 0.18$ (b). Solid blue curve is the unstable manifold of the periodic rectangle orbit. The green curve is the line of constant 55° (a) and 48° (b) emission direction into the farfield. The thick black lines mark the end of the circle segments of the boundary and coincide with discontinuities in the manifolds.

emission with a peak direction (55°) slightly shifted from the quadrupole; the narrowness of the farfield peak in the stadium is comparable to that of the farfield peak in the quadrupole. We can associate this peak with the slope and position of the manifold of the unstable rectangular orbit in the stadium, Fig. 20a). The noticeable shift between the $\varepsilon = 0.12$ and $\varepsilon = 0.18$ deformation (see inset in Fig. 19) originates from the change in the slope of the unstable manifold of the rectangular orbit, Fig. 20b). The discontinuities of slope in the unstable manifolds of the periodic orbits in the stadium

result from its non-smooth boundary. These results indicate clearly that a fully chaotic dielectric resonator can nonetheless sustain highly directional lasing modes. It would be interesting to test this in future experiments.

4.5. Tunneling versus refractive directional emission

We have seen in the previous sections that low-index ARC polymer lasers exhibit highly directional emission at high deformations with emission patterns that are extraordinarily sensitive to the specific shape of the boundary. The observations and simulations of directional emission at such high deformations in the quadrupole ARC indicate clearly that such modes are supported by the chaotic component of the ray phase space and emit in a manner determined by the chaotic phase space flow (specifically determined by the unstable manifolds of short periodic orbits as just discussed). Very recent experiments by Lacey *et al.*²⁸ on fused silica microspherical ARCs complement the lasing experiments nicely by looking at low deformations in which the phase space flow is non-universal and one can have either refractive emission from chaotic modes or tunneling emission from regular modes. The two types of modes have very different Q-values and farfield emission patterns, with the chaotic modes showing a kind of symmetry-breaking which would be quite surprising for standard resonators. The index of refraction of these systems is $n = 1.45$ and the phase space structures determining the behavior are the same as in the polymer experiments, i.e. the stable and unstable diamond and rectangle orbits in the quadrupole and motion in their vicinity. These experiments are also important as they directly probe resonant elastic scattering from the passive cavity, for which the wave calculations are essentially exact, as opposed to lasing emission from ARCs for which issues of non-linearity and mode selection may contribute to the observed behavior.

In this experimental work deformed spherical ARCs are fabricated by fusing two silica spheres with a CO₂ lasers at different durations of exposure, leading to nearly spherical silica “beads” on a stem with a range of deformations with major to minor axis ratios corresponding to $\varepsilon = 0.01 - .07$. Light is scattered from the spheres using frustrated total internal reflection coupling via an adjacent prism. This allows strong coupling into relatively high-Q modes not accessible via a focused beam input. These shapes lack axial symmetry, which implies that the overall phase space motion is in five dimensions, not three as in the cylindrical or axial-symmetric spherical case. However for small deformations the authors argue that the escape is

dominated by the same phase space structures as in the 2D quadrupole, with the crucial difference that phase space barriers such as KAM tori are not impassable classically, but can be “crossed” by Arnold diffusion in the higher dimensional phase space. The authors admit that surface scattering and other effects may play a major role as well, but the upshot is that while the prism injection excites modes with $\sin \chi_0 \approx 1$ the emission takes place from lower values of $\sin \chi$ determined by the fastest escape channel. The experiments find qualitatively different emission patterns for different deformations which can be explained by the assumption that different 2D resonances dominate the emission in the different cases.

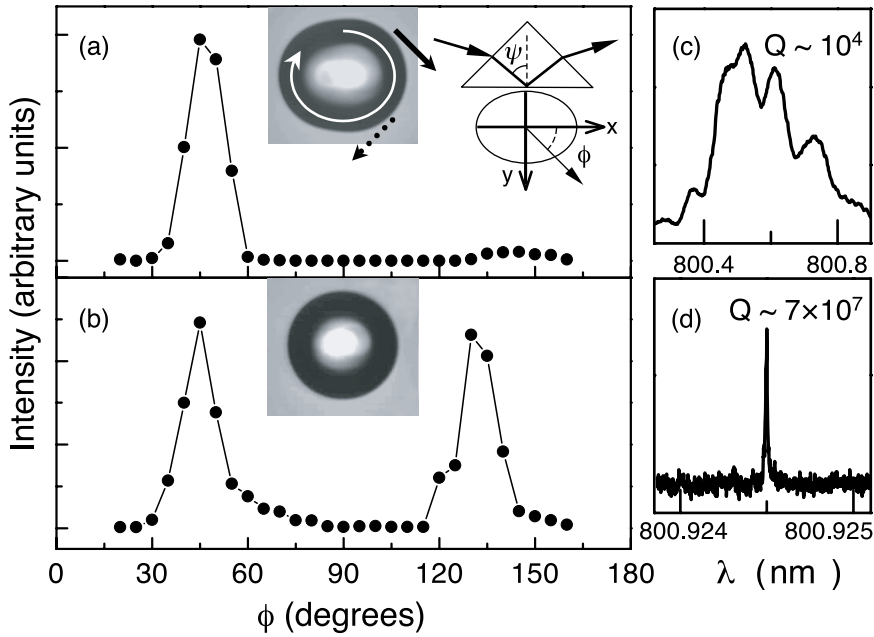


Fig. 21. (a), (b): Farfield emission patterns of WG modes. Insets: bottom view of the resonators showing the progression of shapes in the $x - y$ cross section $\varepsilon = 6.7\%$ and $\varepsilon = 1.2\%$ respectively. WG modes were launched at $\sin \chi_0 \approx 1$. (c), (d): the spectra corresponding to the modes in (a), (b), from which we deduce the Q factors.

Experimental results are shown in Fig. 21 for prism excitation; note that in such a scattering experiment only one sense of rotation of the waves is excited (see inset Fig. 21a). For relatively large deformation ($\varepsilon = 0.067$ is still much smaller than in the polymer experiments reported above) there is a

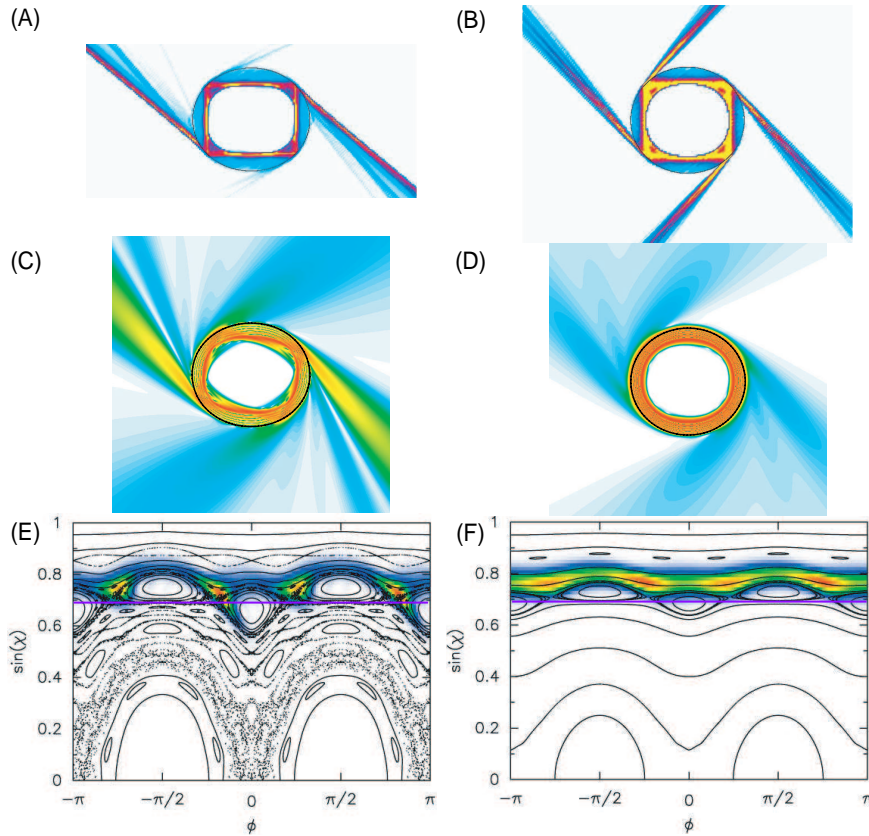


Fig. 22. Ray and wave calculations for modes in the quadrupole with index of refraction $n = 1.45$. Left column has a deformation of $\varepsilon = 0.065$, right column of $\varepsilon = 0.034$. Emission patterns with qualitatively different symmetry are found in agreement with the silica ARC experiments just reported. Top: Intensity pattern of escaping rays with a ray simulation based on a Gaussian bundle of rays around the unstable period four fixed point (A) and a Gaussian bundle above the separatrix (B). In both cases we used the modified Fresnel formula^{20,39} with $kR = 1000$ which takes into account tunneling corrections due to curvature. We propagate a Gaussian bundle of 6000 rays for 600 reflections. (C) and (D) show intensity pattern of two associated WG modes with $kR = 112.63$ and $kR = 112.452$ respectively. (E) and (F) show the associated Husimi distribution and the SOS. The purple line indicates the critical angle of incidence $\sin \chi_c = 1/n$.

single emission peak in the $\theta = 45^\circ$ (the other symmetric one at $\theta = 225^\circ$ is not visible due to the presence of the prism). This pattern is essentially the same behavior as the polymer ARC lasers at higher deformation when one takes into account the presence of only clockwise circulating waves (note

the authors' opposite convention on the farfield angle such that θ is positive in the fourth quadrant). There is no similar bright emission in the $\theta = 135^\circ$ directions (dashed vs. bold arrows in Fig. 21(a)); hence the pattern breaks the symmetry one might have expected for emission from modes based on the rectangular four-bounce orbit. Note that we have already seen this symmetry breaking in the ARC polymer lasers and understand that it arises from the asymmetry of the stable and unstable directions near this unstable orbit. A very different pattern is seen for samples with lower deformations ($\epsilon = 0.012$); here two equal peaks are seen symmetrically situated around $\theta = 90^\circ$, coincident with much higher Q-factors (Fig. 22(d)). This is consistent with emission from the points $\phi = \pm 45^\circ$ on the boundary as one might expect from a mode based on the rectangle orbit.

The authors²⁸ provide a simple explanation of this difference based on the phase space structure of the quadrupole near the critical line. First, as they emphasize, any non-elliptical deformation of the circle is non-perturbative in that it destroys an infinity of symmetry-related periodic orbits (e.g. squares and rhombi) and replaces them by two periodic orbits (the unstable rectangle and the stable diamond). The size of the stable island of the diamond scales as $\sqrt{\epsilon}$ and not as ϵ and hence is much larger than naive expectations from perturbation theory. Similarly, the separatrix region of chaos near the unstable rectangle orbit will extend over a large range of $\sin \chi \sim \sqrt{\epsilon}$. Hence even very small deformations can give highly directional emission patterns. The authors assume that Arnold diffusion or some other mechanism allows injected rays to emit lower down in the surface of section than their injection angle. With this assumption they offer the following explanation of the data. The non-symmetric emission patterns observed at $\epsilon = 0.067$ are based on refractive emission from separatrix states near the rectangular orbit; the symmetric patterns at lower deformation are based on states slightly higher in the surface of section which do not reach the critical angle and emit by tunneling (evanescent leakage) from points on the boundary symmetrically placed around $\phi = 0$ (see Fig. 22). Such states should have much higher Q (as observed) because they involve leakage from modes which would be totally-internally reflected classically. In Fig. 22 we see examples of such symmetric (tunneling) modes and non-symmetric (refractive) modes calculated numerically, with their respective Q-factors differing as in the experiment. These experiments provide another dramatic indication of the influence of non-perturbative phase space structure on the emission patterns from deformed spheres and cylinders. They are complementary to the polymer ARC laser experiments as the

passive cavity mode emission patterns and Q-values are directly measured, whereas the cavity shapes are not precisely controlled as in the polymer ARCs and the phase-space diffusion mechanism in the 3D cavity is not fully understood.

4.6. Overview of low-index ARCs

To summarize the results of this section: low-index ARC lasers and resonators show dramatic differences between the emission patterns of similarly-shaped devices which can be understood by analysis of the phase-space ray dynamics. These differences are particularly dramatic when comparing integrable shapes such as the ellipse with non-integrable billiard shapes such as the quadrupole. The persistence of highly directional emission in strongly deformed quadrupole ARC lasers was not consistent with the earlier adiabatic model,³¹ and a more recent model¹² in which emission directionality at large deformations is controlled by the geometry of the unstable manifolds of short periodic orbits gave a much better account of the data. Calculations indicate that fully chaotic ARC laser resonators should also give highly directional emission. Recent experiments using prism coupling to passive ARC cavities also indicate the coexistence of modes of different Q-value and very different directional coupling. The nature of this difference arises from the different out-coupling mechanisms (tunneling vs. refractive emission). In all cases, study of the phase space structures in the surface of section gives qualitative explanations of the observed emission patterns and ray models can reproduce semi-quantitatively the experimental and wave-optical results.

5. Semiconductor ARC lasers

In the previous section we reported in some detail experiments on polymer and silica ARC resonators and lasers with index of refraction $n \approx 1.5$. There have in addition been several experiments on deformed liquid droplet lasers.^{40,41,42} In these experiments a universal phase space flow (i.e. a property insensitive to initial conditions in phase space) determined the directional output of the laser. Moreover, all of these have been optically pumped systems and hence not suitable as prototypes for microcavity lasers of technological interest. During roughly the same time period a number of ARC semiconductor lasers have been fabricated and measured, and in two cases these have been electrically-pumped lasers of some potential technological interest. In these systems the index of refraction ranged between

$n = 2.65 - 3.3$ leading to stronger confinement of light rays by (near) total internal reflection, and hence increasing the fraction of phase space accessible to long-lived modes for lasing. In these lasers the nature of the lasing modes were more diverse and the issue of how mode selection occurs was strongly raised (but not yet fully answered). We will review the relevant experiments in roughly chronological order: electrically-pumped quantum cascade ARC lasers first, then optically-pumped GaN ARC lasers, and finally optically and electrically-pumped “spiral” GaN multiple-quantum-well lasers, which are not really ARCs by our definition, but which were a natural outgrowth of the shape design program which began with ARCs.

5.1. Quantum Cascade ARC lasers

The development of efficient semiconductor microlasers is of primary importance for current as well as future photonic or optoelectronic applications. A major milestone in this direction was the development of quantum cascade (QC) lasers by the Bell Labs team of Faist, Cappasso *et al.*⁴³ Typical semiconductor lasers are bipolar in character (i.e. are diodes), meaning that the laser action is fed by the *interband* electron-hole transitions of a semiconducting heterostructure involving doped and undoped III-IV semiconductors such as GaAs, InAs, GaN. Quantum Cascade lasers on the other hand are *unipolar* and employ the electronic inter-subband transitions between quantized conduction band states in a multiple quantum well structure. The unipolar character of QC lasers excludes non-radiative combination of electrons and holes which is a major problem with diode lasers when one wants to access shorter or longer wavelengths other than the typical communication window of about 1.3-1.5 μm . Another attractive feature of the QC devices is their versatility in emission wavelength. Different transition energies can be realized by adjusting the individual layer thicknesses without changing the composition of the constituent materials, covering virtually the complete infrared spectral region ($\lambda \sim 3\text{-}25 \mu\text{m}$).

While the ever-improving semiconductor quantum-engineering technology is an important factor in increasing the efficiency of these miniature lasers, the optimization of the geometric shape of the resonator plays also a major role. The study of ARC microcylinder QC lasers was undertaken along these lines in a 1997 collaboration between Yale and Bell labs leading to the exciting results reported in Gmachl *et al.*⁷

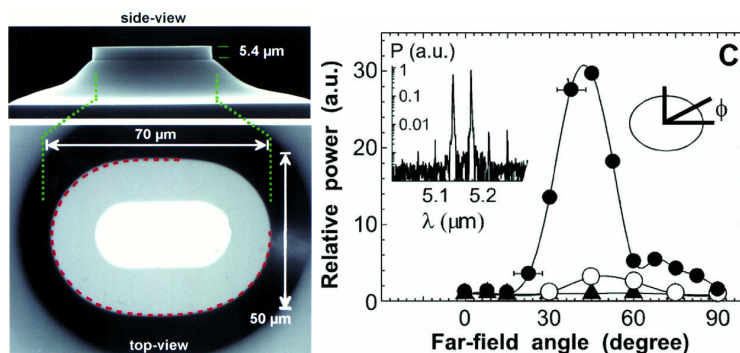


Fig. 23. (a) Scanning electron micrographs of the top and side-view of one of the deformed cylindrical quantum cascade microlasers. (b) Angular dependence of the emission intensity for deformations $\epsilon = 0$ (triangles), $\epsilon = 0.14$ (open circles), $\epsilon = 0.16$ (filled circles). The right inset shows the coordinate system used and the left inset shows the logarithmic plot of the measured power spectrum. The FSR of the peaks is found to agree with the calculated bowtie FSR (after Ref. 7).

5.1.1. Directional emission from stable bowtie modes

To test the effect of deformation on the lasing properties, a set of microcylinder lasers of increasing quadrupolar deformation were fabricated and tested on the same chip.⁷ It was found that while for lower deformations the emission is more or less isotropic, above a deformation of about $\epsilon = 0.14$ a large anisotropy rapidly developed. At $\epsilon = 0.16$, the emission pattern peaked at about 45° with a maximum to minimum ratio of about 30 : 1 (see Fig. 23). While the low deformation data were consistent with emission from whispering gallery modes, it was clear that a mode of a different character was dominating the emission at higher deformations. There were two experimental clues which were available for the determination of the lasing mode:

- Sudden onset of directionality above a deformation of $\epsilon = 0.14$.
- The existence of six equally spaced peaks in the measured spectrum at maximum power.

From the standpoint of ray dynamics, the main difference between semiconductor ARCs and lower index polymer ARCs analyzed in the previous section is their typically higher index of refraction. For the material system used in the above experiment (InGaAs/InAlAs), the effective index of refraction was $n \sim 3.3$. Such a large index of refraction makes available a larger portion of the SOS available for the support of long-lived

resonances. Particularly, the lower portion of the phase space close to the critical line ($\sin \chi \sim 0.3$) is a regime which is subject to more (classical) non-linearity and hence chaos than the higher lying WG region (as a simple measure, the effective ‘kick strength’ of the quadrupole billiard map goes as $(1 - \sin^2 \chi)^{3/2}$).³⁹ Therefore the difference between stable and chaotic motion is enhanced for intermediate deformations in this part of the SOS, where large islands of stable motion and strong chaos coexist.

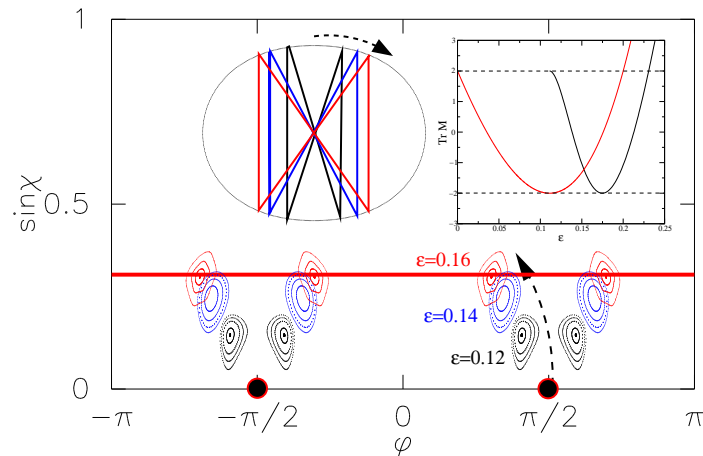


Fig. 24. Illustration of the motion of the bowtie island with changing deformation. Drawn in red is the critical line. Inset shows the stability diagram of the bouncing ball and bowtie orbit as given by the variation of the trace of the monodromy matrix M . For $|TrM| > 2$ an orbit is unstable, hence one sees that motion in the vicinity of the bowtie orbit is stable for $0.11 < \epsilon < 0.23$. The bouncing ball restabilizes after the bifurcation and only becomes unstable at $\epsilon \approx 0.2$; a non-generic behavior which is possible due to the discrete symmetry of the billiard.

The observation of rather sudden onset of directional emission suggested a mode which (unlike the whispering gallery modes) is not continuously connected to zero deformation. In fact, there is one clear candidate, the stable bowtie orbit, that does not exist below a deformation of $\epsilon = 0.11$. For all ARCs there is a large stable two-bounce (“bouncing ball”) orbit which appears non-perturbatively for small deformations and which typically destabilizes as the deformation increases. The bowtie orbit arises as a byproduct of the destabilization of the bouncing ball orbit; it is “born” through a period doubling bifurcation of this orbit at $\phi = \pm\pi/2$ (see Fig. 24). Below a deformation of about $\epsilon = 0.14$, the corresponding bowtie resonances are

too leaky to provide efficient laser feedback, because as seen from Fig. 24, the stability island of the bowtie orbit is far below the critical line. However, further deformation slowly moves the island up in $\sin \chi$ until at about $\epsilon = 0.16$, when the critical line is reached and the data indicate that its associated mode becomes the favored lasing mode. Since the stable bowtie motion is strongly localized (Fig. 25) in position and space, it leads to highly directional emission. Properties of modes based on stable ray motion close to a periodic orbit are amenable to an analytic study through a generalized Gaussian optical description.¹⁵ Quite similar to the sequence of Gauss-Hermite modes found in a stable Fabry-Perot cavity, it's possible to associate a sequence of modes with an island of stable motion. To lowest order, the resonance frequencies and lifetimes of these modes are functions of the index of refraction n , the length of the orbit L and the radius of curvature at each bounce b of the periodic ray orbit, $\{\rho_b\}$, and the corresponding impact angles $\{\sin \chi_b\}$:

$$\text{Re}[nkL] = 2\pi m + \text{mod}_{2\pi} \left[\left(\frac{1}{2}N + N_\mu \right) \pi \right] + \left(n + \frac{1}{2} \right) \varphi + \varphi_f \quad (21)$$

$$\text{Im}[nkL] = -\gamma_f \quad (22)$$

where $\varphi_f = \text{Re}[-i \sum_b^N \log \left[\frac{n\mu_b - 1}{n\mu_b + 1} \right]]$ and $\gamma_f = \text{Im}[-i \sum_b^N \log \left[\frac{n\mu_b - 1}{n\mu_b + 1} \right]]$. μ_b is the ratio of incidence angle to transmitted angle $\cos \chi_i / \cos \chi_t$ calculated from Snell's law at each bounce b , φ is the stability angle for the particular periodic orbit, N is the number of bounces and N_μ is the Maslov index which depends on the topology of the phase space motion.¹⁵ The resulting spectrum contains two distinct constant spacings. Here, the longitudinal mode index m gives rise to a FSR $\Delta k_{long} = 2\pi/L$ and the transverse index n results in a shorter FSR of $\Delta k_{trans} = \varphi/L$. Because of the symmetry of the resonator shape under reflections with respect to its minor and the major axes, the solutions can be classified into four different classes. Each class is distinguished by the parity of the corresponding solutions under the reflection operations, denoted by $++$, $+-$, $-+$ and $--$. For instance the solution $+-$ has even parity under reflection with respect to the long axis, and odd with respect to the short axis. The Gaussian theory predicts¹⁵ that for the bowtie mode, solutions with identical parity with respect to the *short axis* form degenerate doublets, and that these two parity types ($++$, $+-$) and ($--$, $-+$) alternate in the spectrum every FSR. A group theoretical analysis of the symmetry properties of the *exact* solutions however shows that the degeneracy is not exact. In fact, the exact quasi-degenerate solutions display an exponentially small (in k) splitting. As seen in Fig. 25,

these arguments reproduce the exact (numerical) spectrum quite well.

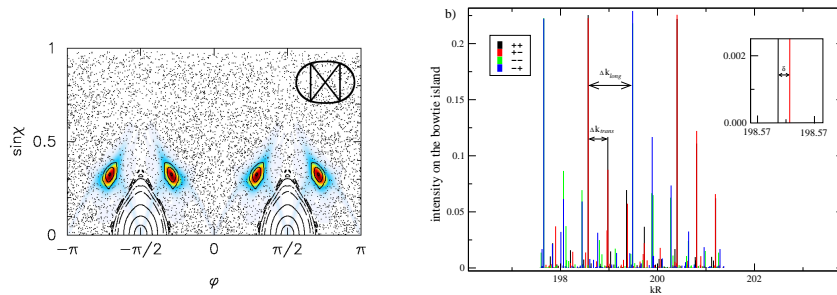


Fig. 25. (a) (Left) Surface of section for quadrupole billiard at deformation of $\epsilon = 0.17$ which supports a stable bowtie orbit (see inset) leading to four islands in the SOS. A numerical solution of the resonance problem is Husimi-projected onto the SOS and is plotted in color scale; it localizes on the island and is a stable bowtie mode. (b) Spectrum weighted by overlap of the Husimi projection of the solutions in a spectral range with the bowtie island. Note the emergence of regularly spaced levels with two main spacings Δk_{long} and Δk_{trans} . These spacings, indicated by the arrows, are calculated from the length of the bowtie orbit and the associated stability angle (see Eq. (21)). The color coding corresponds to the four possible symmetry types of the solutions, as explained in the text. In the inset is a magnified view showing the splitting of quasi-degenerate doublets. Note the pairing of the $(++)$ and $(+-)$ symmetry types. The different symmetry pairs alternate every FSR (Δk_{long}).

The observed lasing spectrum in the experiments shows six equally spaced peaks (see Fig. 23), with a FSR of $\Delta\lambda = 40.4 \text{ nm}$. This spacing is approximately equal to the longitudinal FSR ($\Delta\lambda_{long} = 39.5 \text{ nm}$) calculated from Eq. (21), indicating that it was a particular transverse mode which was lasing for different values of m . For comparison, the transverse mode spacing expected from Eq. (21) is about $\Delta\lambda_{trans} = 2.2 \text{ nm}$ and the splitting of quasi-degenerate resonances is about $\Delta\lambda_{split} \approx 0.1 \text{ nm}$. Just by looking at the spectrum it's not possible to discern which transverse mode or which symmetry class is lasing. At this point, the farfield emission pattern can be used to pinpoint the lasing mode. A crucial point here is that each spectral peak is expected to be formed through locking of the quasi-degenerate modes corresponding to two different symmetry classes. It has been shown both theoretically^{44,45} and experimentally⁴⁶ that if eigenfrequencies of the modes participating in the non-linear lasing process are close enough, locked behavior can occur leading to stationary output intensity pattern. This is called *cooperative frequency locking*. The resulting non-linear modes are linear combinations of the participating modes and

may display asymmetric emission patterns despite the fact that the resonator is symmetric (a good example of spontaneous symmetry breaking). To compare to the experiments, we plot in Fig. 26 linear combinations of the quasi-degenerate transverse modes close to the central lasing frequency. The farfield emission pattern observed in the experiments is found to be in conformity with that of the transverse doublet $m = 2$. Note that the resulting emission pattern peaks at a point away from what is expected from Snell's law applied to the bowtie orbit. These findings were reinforced by experiments by the TU-Wien group⁴⁷ on QC GaAs/AlGaAs microlasers emitting around $\lambda = 10 \mu\text{m}$. The boundary deformations investigated in this work were again quadrupolar and the effective index of refraction around $n_{eff} \approx 3.2$. Emission patterns observed were of two distinct types, one of which was found to correspond to that of the bowtie mode. The robustness of the emission pattern to a change in lasing wavelength is a testament to the effectiveness of inferences based on short-wavelength approximations and ray-optical phase space. As long as the resulting phase space (and the index of refraction) is identical, similar farfield patterns are expected regardless of the wavelength and the size of the resonator (provided $nkR \gg 1$; in the Bell Labs-Yale experiment $nkR \sim 120$ and in the TU Wien experiment $nkR \sim 100$).

Although numerical work and physical arguments allowed us to identify this mode after the experiment, we have no predictive theory for the mode selection in this case. The second excited bowtie mode is not the highest Q mode of the cold cavity, nor is it particularly selected by the peak of the gain curve, which is broad enough to allow other modes to lase.

5.1.2. *Power increase and mode selection in ARCs*

The issue of mode selection in ARCs is made more salient because of the second major finding of the Bell Labs experiment. Not only did the bowtie laser provide highly directional emission, improving the brightness (power into a given solid angle) of the laser by a factor of order 30; but the deformed lasers produced more than a thousand times the output power of the identically-fabricated circular lasers.⁷ The demonstrated high output power and directional emission solve major problems with earlier semiconductor microdisk lasers and makes their use technologically promising.

The difference in peak output power between the ARC and circular cylinder lasers is interesting theoretically and not yet explained. The peak output power certainly depends on the non-linear properties of the las-

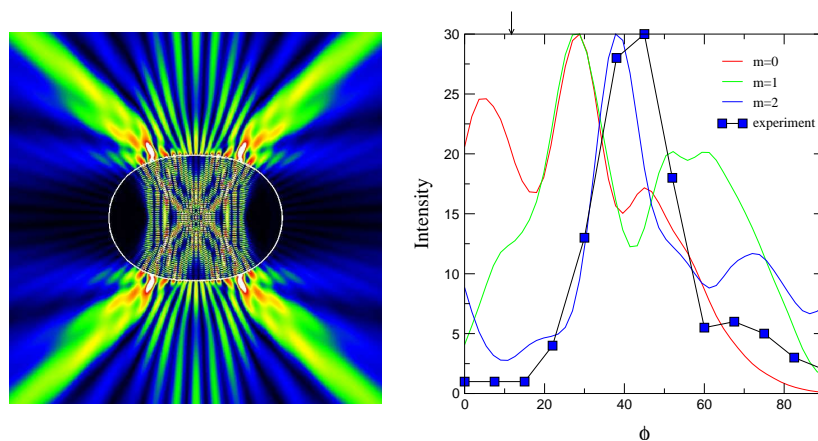


Fig. 26. (a) The numerically calculated resonance corresponding to the $m = 2$ bowtie-mode at $\epsilon = 0.16$ that is consistent with the observed spectrum and emission pattern. (b) Comparison of experimental data for $\epsilon = 0.16$ to numerically determined farfield patterns for the $m = 0$, $m = 1$ and $m = 2$ transverse modes of the bowtie resonance. We have plotted linear combinations of quasi-degenerate doublets close to $nkR = 120$. The peak transmission is in good agreement with the $m = 2$ transverse mode. The arrow points to the peak angle expected from ray optics, i.e. refracting out of the bowtie-orbit using Snell's law.

ing and is not a property of a given mode of the linear wave equation. The standard and well-verified model of the power output of a single-mode Fabry-Perot laser¹⁴ finds that the power output is optimized for a given pump power when the external cavity loss (which is the width we are calculating) equals the internal cavity loss (neglected in our model). One may conjecture then that the bowtie optimizes the power output, even though it is not the highest Q mode. However this observation is not sufficient to explain the experiment. The circular lasers measured have a range of Q-values corresponding to different radial quantum numbers for a given angular momentum. In particular, there should exist modes with Q very near that of the bowtie. The main difference between circular and ARC lasers is that in the circular case this mode will strongly overlap in space with other higher Q modes; whereas in the ARC strong chaos has wiped out the competing higher Q modes in the vicinity of the bowtie. Therefore we conjecture that it is the lack of mode competition in bowtie lasers which allows it to optimize its output power. The experiment provides some modest support for this conjecture as the circular lasers are consistently found to lase on several modes simultaneously, whereas the ARC lasers are single

mode unless they are pumped very hard.⁷ Work is underway to analyze mode competition in chaotic lasers and verify these speculations.

Both of the experiments and the accompanying theoretical analysis indicate that the geometrical shaping of the resonator is an important parameter in the design of efficient miniature laser devices. It was demonstrated that by merely optimizing the shape of the resonator, it's possible to increase the optical output power by three order of magnitude and simultaneously obtain a directionality emission asymmetry of 30:1.

5.1.3. *Anomalous Q-values of stable ARC modes: a new signature of chaos*

We close this section by reporting a dramatic prediction of the wave chaos theory relevant to stable orbit modes, but not yet tested experimentally. This prediction is not relevant to the QC ARC lasers just mentioned for which the stable orbit is right at the critical angle, but will be very relevant for modes which are totally internally reflected (TIR). In Section (5.1.1) above we have noted that the discrete symmetry of quadrupole ARCs (as opposed to the continuous symmetry of circular resonators) precludes the existence of exactly degenerate stable (or unstable) modes, despite the fact that such degeneracies are predicted to occur within the Gaussian optics approximation for the stable modes. This is a well-known shortcoming of semiclassical methods which at leading order do not resolve exponentially small effects due to tunneling, and this short-coming applies to both integrable ARCs, such as the ellipse, as well as the (generic) non-integrable ARCs. However it has been predicted^{15,48} that the absolute size of these tunneling effects are dramatically sensitive to the presence or absence of chaos in parts of the phase space away from the stable islands which give rise to Gaussian modes. We will not attempt to go into any details of the theory here; they can be found in Refs. 15, 48. The qualitative physics is the following. Consider any stable periodic orbit which is not self-retracing; there will exist an independent Gaussian mode series with a distinct field pattern corresponding to the two senses of traversing the orbit, and within the Gaussian theory these two series will be exactly two-fold degenerate. However there is some small tunneling probability for a ray circulating in one sense to eventually reverse its sense of circulation. This tunneling between different stable motions at the same energy has been termed *dynamical tunneling*.⁴⁹ More formally, taking symmetric and anti-symmetric combinations of the two wavefunctions just mentioned will lead to two

states of slightly different energy/frequency (differing by twice the tunneling rate as in the familiar double-well problem). For objects without continuous symmetries this rate will always be non-zero, but its value will depend strongly on the nature of the surrounding phase space. Specifically for stable island modes surrounded by a chaotic “sea” the tunneling rate is parametrically larger than in a comparable integrable system, leading to a much large splitting of the Gaussian modes in the closed system.¹⁵ However these splittings may still be difficult to resolve experimentally.

Very recently, Narimanov⁵⁰ has pointed out that this enhanced tunneling rate, known as “chaos-assisted tunneling” (CAT), will have dramatic observable consequences for ARCs with totally internally reflected stable orbit modes (TIRSO modes). Here the signature of the effect is in the Q-values of the modes and not in the splittings, and the effect can be seen in comparison to circular resonators with zero splitting of the comparable modes. As reported above,²⁸ it is possible to couple to totally-internally reflected modes of passive dielectric cavities using prism coupling. According to the new prediction of CAT theory for ARCs the measured Q-values of TIRSO modes will be orders of magnitude smaller than for the same angle of insertion in the circular cavities. Moreover, the Q-values of TIRSO modes will fluctuate rapidly between different resonances in the same longitudinal sequence while no such fluctuations will be observed for the circular case. This is the signature that escape from the stable orbit modes of ARCs is mediated by tunneling into the chaotic states of the resonator prior to escape into the farfield, whereas no such escape mechanism exists for circular resonators. As the phenomenon of chaos-assisted tunneling in wave-chaotic systems has had few if any experimental demonstrations, it is hoped that experiments of this type will be attempted in the future.

5.2. Diode ARC lasers

Our arguments and examples up to this point indicates that a key requirement for a resonant mode to be the dominant observed mode of a laser is that its weight in the SOS (as measured e.g. by Husimi projection) be concentrated near the critical line for refractive escape. Hence, the investigation of the classical phase space structures in the vicinity of critical reflection gave us a quick and crude estimate of the emission directionality. Particularly, islands of stable motion in the vicinity of critical incidence can lead to localized modes with highly directional emission, as was the case for the bowtie modes of the previous section. One of the intriguing and

well-studied results of quantum chaos theory is the existence of localized modes based on *unstable* periodic orbits, known as *scarred states*.^{51,52,53} If such an orbit is trapped by near total internal reflection near the critical line it may lead to an “unstable” lasing mode. Exactly such a situation was realized in semiconductor diode microlasers studied by Rex *et al.*¹¹ We will now review this experiment and discuss its theoretical interpretation.

In these experiments, microlaser devices were produced by growing GaN on a sapphire substrate, and etching the resulting wafer using a mask and standard photolithography into a $2\mu\text{m}$ high pillar with a quadrupolar deformation of the cross-section, $r(\phi) = R_0(1 + \epsilon \cos 2\phi)$ where $R_0 = 100\mu\text{m}$ (see Fig. 5.2). The resulting structure, which has an index of refraction $n = 2.65$, is optically pumped at 355nm normal to the plane of the pillar and emits at 375nm . Light emitted from the side-walls is collected through an aperture subtending a 5° angle, passed through a lens and detected by a CCD camera in the farfield to yield two-dimensional image data plots of the type described above in Section (3.1).

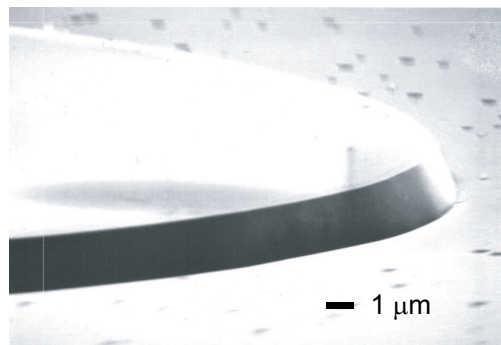


Fig. 27. (a) A scanning electron micrograph of the GaN resonators used in the experiments. The device in the figure has a diameter of $200\mu\text{m}$.

We will now focus on the data collected for $\epsilon = 0.12$ quadrupoles. Note that this is the deformation at which the polymer cylinder lasers discussed earlier emitted at roughly a 35° direction to the major axis, with a boundary image showing a single bright spot on the boundary at negative values of sidewall angle ϕ which correlated well with the farfield peak if one assumed tangent emission. The imagefield for the GaN quadrupole lasers is displayed in Fig. 28(a) and the farfield is shown in Fig. 28(b).

The data show a very different emission pattern than the polymer lasers

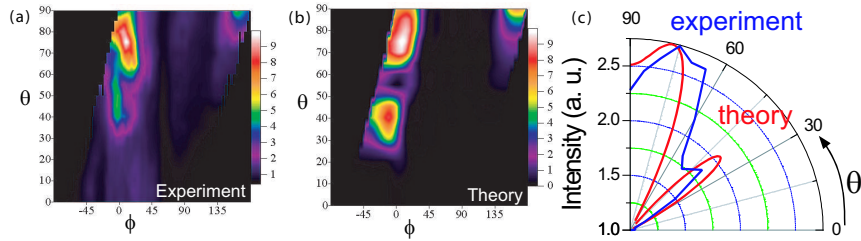


Fig. 28. (a) Experimental data showing in color scale the CCD images (converted to sidewall angle ϕ) as a function of camera angle θ . Three bright spots are observed on the boundary for camera angles in the 1st quadrant, at $\phi \approx 17^\circ, 162^\circ, -5^\circ$. (b) Calculated image field corresponding to the scarred mode shown in Fig. 31. (c) Calculated and experimental farfield patterns obtained by integrating over ϕ for each θ .

of the same shape, demonstrating the crucial role of the refractive index in determining the lasing mode selected. For the GaN lasers the maximum intensity in the 1st quadrant is observed at angle $\theta \approx 74^\circ$ and correlates with emission from the region of the sidewall around $\phi \approx +17^\circ$. The data also show a secondary bright spot at slightly negative $\phi \approx -5^\circ$ and another one at $\phi \approx 162^\circ$ which do not lead to strong maxima in the first quadrant in the farfield. The observation of a small number of well-localized bright spots on the sidewall suggests a lasing mode based on a short periodic ray trajectory. In Fig. 29, we have indicated the approximate positions of the four bright spots on the boundary (the imagefield can be unfolded to the range $\theta = 0 \dots 2\pi$ using the symmetry of the quadrupole). The imagefields for the polymer lasers showed more bright spots and a variable number of them, inconsistent with a single short periodic orbit. In the same figure is shown a view of the SOS at this deformation.

The only stable structures which would result in localized modes in the framework of the previous section, are the bouncing ball and the bowtie islands. For comparison, the stable bouncing ball mode would emit from $\phi = 90^\circ$ in the direction $\theta = 90^\circ$. The stable four-bounce bowtie mode, dominant in the devices of Ref. 7, is also ruled out by our data. It is very low-Q at this deformation due to its small angle of incidence and would give bright spots at $\phi = 90^\circ \pm 17^\circ$, far away from the brightest spot at $\phi = 17^\circ$ (see Fig. 29). There is however a pair of symmetry-related isosceles triangular periodic orbits with bounce points very close to the observed bright spots (see Fig. 29). The two equivalent bounce points of each triangle at $\phi = \pm 17^\circ$ and $180^\circ \pm 17^\circ$ have $\sin \chi \approx 0.42$, very near to the critical value, $\sin \chi_c = 1/n = 0.38$, whereas the bounce points at $\phi = \pm 90^\circ$ have

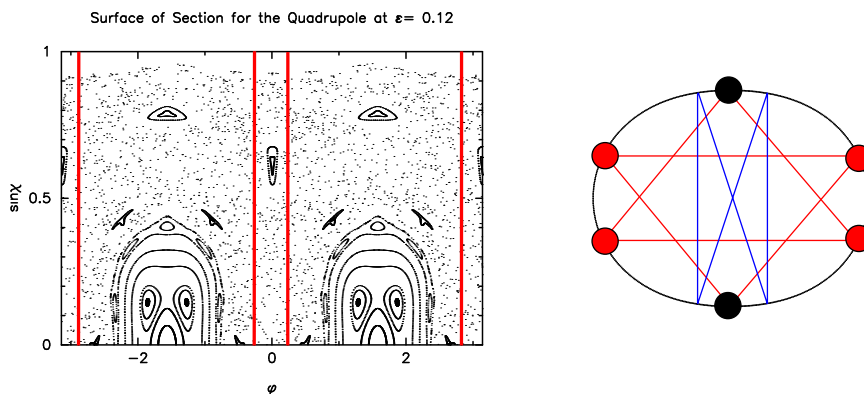


Fig. 29. The SOS of the quadrupolar billiard at a deformation of $\epsilon = 0.12$. The red vertical lines indicate the values of ϕ at which the bright spots in the imagefield are observed. On the right is a schematic indicating in red the experimental bright spots in the real space. The location of these spots is strongly inconsistent with the bowtie orbit at this deformation but is consistent with modes based on the two triangle orbits shown. These orbits would have the two “dark” bounce points (indicated in black) that are well above total internal reflection for the index of $n = 2.65$

$\sin \chi = 0.64$ and should emit negligibly (Fig. 29). This accounts for the three bright spots observed experimentally in Fig. 28(a) (the fourth spot at $\phi \approx 197^\circ$ is completely blocked from emission into the first quadrant). Note furthermore the proximity of the four emitting bounce points to critical incidence; a simple application of Snell’s law to these rays would lead to farfield maxima in reasonable agreement with the observed peaks in the farfield distribution Fig. 28(c) (however not with the imagefield data, see below).

These basic observations could be explained with generalized Gaussian modes of the previous section, were it not for the fact that the triangular periodic orbit is unstable at this deformation. In Fig. 30, we plot the trace of the monodromy matrix as a function of deformation, which shows that at deformation $\epsilon = 0.12$, $Tr(M) = -5.27$. The triangular periodic orbit is unstable with a Lyapunov exponent of $\lambda \approx 1.62$ (see Fig. 30). We have remarked in Section 5.1 that our method of constructing a localized mode on a periodic orbit fails, if the orbit is unstable. Failure of the method however doesn’t mean that localized modes do not exist. In fact, numerical solution of the quasi-bound states at this deformation, using the method of Section 2.4, finds modes localized on the triangular orbit, as seen in the configuration space plot in Fig. 31(a). A much clearer picture, free of in-

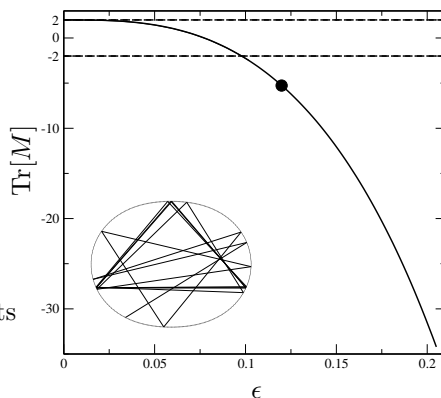


Fig. 30. The variation of the trace of the monodromy matrix with respect to the quadrupolar deformation ϵ . The black circle indicates the experimental value $\epsilon = 0.12$, at which $\text{Tr}(M) = -5.27$. The two dashed lines delimit the regime $-2 < \text{Tr}(M) < 2$ at which the triangular orbit is stable. In the inset is shown real space simulation of a ray orbit started with initial conditions which are away from the triangle fixed point at least by $\delta\phi = 10^{-3}$, $\delta\sin\chi = 10^{-4}$, followed for 20 bounces.

terference fringes, is provided by the Husimi plot of this mode in Fig. 31 projected onto the SOS. The brightest spots clearly coincide with the triangular fixed points, and the whole density is localized in the midst of the chaotic sea. This mode is an instance of a *scarred state* and is one of the most surprising and esoteric objects of quantum chaos theory.

Note however that the numerical calculations are performed at $nkR \approx 129$, whereas the experimental lasing frequency corresponds to $nkR \approx 4400$. Despite this difference of more than one order of magnitude, the agreement between experimental results (farfield and imagefield) and simulation is quite good. To understand this we need to discuss some further aspects of scarred modes.

“Scarring” refers strictly to the imprint left by *unstable* periodic orbits in a *group* of states.⁵¹ There is still a lot of discussion about the quantification of this imprint,⁵³ but for our purposes here, the simplest and most intuitive of such measures is the enhancement of eigenstate intensity along (a tube surrounding) a given unstable periodic orbit and its invariant manifolds (the latter is best measured in the SOS). Understanding the phenomenon of scarring requires a major departure from the approaches of EBK and Gaussian optics which allow construction of individual modal solutions of the wave equation. Scarring on the other hand refers to a statistical phenomenon. It’s a statistically significant correction to Berry’s conjecture⁵⁴ that for er-

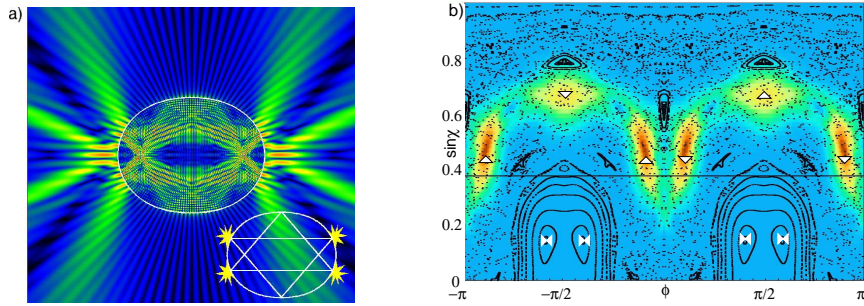


Fig. 31. (a) Real-space false color plot of the modulus of the electric field for a calculated quasi-bound state of $nkR_0 \approx 129$ (n is the index of refraction, k is the real part of the resonant wavevector) and $\epsilon = 0.12$ which is scarred by the triangular periodic orbits shown in the inset (M. V. Berry has termed this the “Scar of David”). The four points of low incidence angle which should emit strongly are indicated. (b) Husimi (phase-space distribution) for the same mode projected onto the surface of section of the resonator. The x-axis is ϕ_W and the y-axis is $\sin \chi$, the angle of incidence at the boundary. The surface of section for the corresponding ray dynamics is shown in black, indicating that there are no stable islands (orbits) near the high intensity points for this mode. Instead the high intensity points coincide well with the bounce points of the unstable triangular orbits (triangles). The black line denotes $\sin \chi_c = 1/n$ for GaN; the triangle orbits are just above this line and would be strongly confined whereas the stable bowtie orbits (bowtie symbols) are well below and would not be favored under uniform pumping conditions.

godic systems (in the short-wavelength limit), individual eigenstates will cover uniformly all the available energy hypersurface (translated to optical resonators, this means that the local angular spectrum calculated at any point in the resonator will contain all the possible directions uniformly), up to uncorrelated Gaussian fluctuations. In the extreme short-wavelength limit no individual mode of the wave equation will localize on an unstable periodic orbit. Instead, the effect of a short periodic orbit and its associated hyperbolic manifold will be seen in a group of eigenstates in an energy range Δk , where $\Delta k \sim u/L$ (here u is the Lyapunov exponent and L is the length of the orbit). The broadened spectral peaks corresponding to these states repeat periodically with a period of $2\pi/L$. Since the average density of states of a 2D or 3D optical resonator increases with k once $kR \gg 1$ there will be many states under this broadened peak and no single state will be strongly localized on the periodic orbit; the additional statistical weight will be carried by many of them. In systems of the type we are considering there are an infinite number of periodic orbits, however the effect of longer orbits on the spectrum and modes is less significant, because they are more unstable: $\Delta k \sim u/L \sim \text{constant}$ whereas the spacing of the peaks $\sim 1/L$

so the the broadening becomes much larger than their spacing and no local density of states oscillations are observable. For the short and not very unstable periodic orbits one finds that the averaged wavefunction magnitude over this range Δk (and space) is found to display a strong enhancement in space in the vicinity of the particular periodic orbit with a form depending only on the parameters of the ray orbit and a simple scaling with k .⁵⁵ Along similar lines, for optical resonator modes, the farfield averaged over a given wavelength (spectral resolution of the spectrum analyzer) and spatial range, would display clearly the effect of a single short periodic orbit and its linear manifolds. Our numerical solution in Fig. 31 at low nkR is a good representation how an *averaged* wavefunction and emission at higher nkR would manifest, because at lower nkR the range $\Delta k \sim u/L$ will contain only a few modes and a single mode can be a “strong scar”. One may also conjecture that the effect of non-linear mode locking may work to create a single non-linear scar out of many nearby modes in the actual lasing system. Therefore a scarred mode, or multi-mode lasing emission consistent with scarring is a reasonable explanation of the data.

However closer inspection of the imagefield in Fig. 28(a) presents an intriguing puzzle from the point of view of ray optics. A mode localized on these triangular orbits might be expected to emit from the four bounce points approximately in the tangent direction according to Snell’s law; this means that the bright spot at $\phi = 17^\circ$ should emit into the direction $\theta \approx 115^\circ$ (Fig. 5.2), whereas the data clearly indicate that the $\phi = 17^\circ$ bright spot emits in the direction $\theta = 72^\circ$. (Note that the Snell’s law argument worked well for the polymer lasers studied above). Thus the emission pattern here violates the intuitive expectations of ray optics by 43° , a huge discrepancy (see Fig. 5.2). Moreover, $\lambda/nR = 2.8 \times 10^{-3}$, so we are far into the regime in which the wavelength is small compared to the geometric features of the resonator and ray optics would be expected to be a good approximation. To ensure that this discrepancy did not arise from some error in the experimental imagefield we simulated the full experimental setup, starting with our numerically-determined scarred solution (Fig. 31(a)) inside the resonator and propagating it through an aperture and lens into the farfield, reproducing the expected imagefield. The way to do this is described in Ref. 20. The imagefield corresponding to the numerical resonance calculated in this manner is reproduced in Fig. 28(b). The good agreement with the experimental data in Fig. 28(a) indicates that the effect is real and is robust over a range of wavelengths.

The physical mechanism for this surprisingly large violation of ray op-

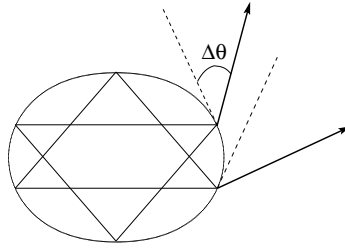


Fig. 32. Schematics showing the three emitted “beams” detected in the experiment (solid lines) and illustrates their strong deviation from Snell’s law (dashed tangent lines).

tics was given in Refs. 11, 56. From the numerical data of Fig. 31(b), it is clear that the scarred mode, while localized around the triangle orbit, has a significant spread in angle of incidence, $\Delta \sin \chi \approx 0.2$. This means that we must regard the scarred mode as a bounded beam with a large angular spread, with some components almost totally reflected and other components transmitted according to the Fresnel transmission law. It was shown^{11,56} that such a beam incident on a dielectric interface is strongly deflected in the farfield away from the tangent direction expected from a naive application of Snell’s law resulting in Fresnel Filtering (FF). The farfield peak-shift, $\Delta\theta_{FF}$, depends on the beam width Δ and on n ; analysis of the stationary phase solution gives the result that, for incidence at critical angle χ_c ,

$$\Delta\theta_{FF}^c \approx (2/\tan \chi_c)^{1/2} \Delta^{-1/2} \quad (23)$$

It’s clear this effect will be crucial for analysis of the emission patterns of dielectric microlasers, because the dominant lasing mode will be often based on long-lived and localized quasi-normal modes which always involve ray components close to the critical incidence. Furthermore, even if the experiments are performed deep in the short-wavelength limit $nkR \rightarrow \infty$, localization (in SOS, per coordinate) will be of order $1/\sqrt{nkR_0}$ (as is for stable island modes for example) leading to a spectral width $\Delta \propto \sqrt{nkR_0}$, so from Eq. (23), the deviation angle at critical incidence $\theta_{FF}^c \propto (nkR)^{-1/4}$ and hence may be large for $nkR \sim 10^2 - 10^3$, as in recent experiments on semiconductor ARC lasers.^{7,47,11}

Evidence for laser action on a triangular scarred state was also obtained in the Bell Labs experiments on a series of quadrupolarly deformed semiconductor diode (GaInAs quantum wells embedded in GaAs/GaInP waveguide) lasers with an effective index of refraction $n_{eff} = 3.4$. There

were three interesting features of this experiment. First, with the given index of refraction and a quadrupolar boundary deformation $\epsilon \approx 0.16$, one would expect to observe emission from the stable bowtie modes, because the situation is almost identical to the QC ARC experiment of the previous section. However this is not the case because of the preference of the device towards TE polarized modes. In the QC laser intersubband optical transitions lead to a selection rule which allows light emission only in the 2D plane with TM polarization normal to the quantum well layers.⁷ Because of the existence of the Brewster angle for TE polarization, the reflectivity of the boundary drops practically to zero for the TE version of the bowtie mode before again rising sharply to TIR close to critical angle. Therefore, the bowtie modes in diode lasers are considerably leakier than their TM counterparts in QC lasers and apparently are not selected as the lasing modes. The second notable observation was the nature of transition from lasing via regular modes to chaotic modes with increasing deformation. Because imaging or farfield data was not available, they looked for a signature of this transition in the spectral data. Above a deformation of about $\epsilon = 0.03 - 0.06$ (which coincides approximately with the KAM transition close to the critical line), the spectrum displayed evenly spaced mode doublets with large splitting, which are absent in low deformation data. The FSR of the doublets are found to be consistent with a triangular periodic orbit of the type seen in the Yale GaN experiments and the authors attribute the relatively large splittings to boundary roughness. Considered as a perturbation, boundary roughness effects localized modes to a greater extent than extended whispering gallery modes of smaller deformation. The final significant point is that this experiment found a persistence of the lasing characteristics through the stability-instability transition of the triangular orbit, which happens at about $\epsilon \approx 0.1$. It's worth reiterating that while the nature of the mode on the stable side is of Gaussian type, the individual modes based on unstable motion does not yield to a simple analytic description and the resulting scarred states can only be obtained numerically. The numerical solutions are found to yield localized modes on both sides of the transition.

A more direct demonstration of the last observation was provided by Rex *at al.*¹⁰ in an extension of the GaN laser experiments to a range of quadrupole-hexadecapolar deformations, defined by the mathematical equation:

$$r(\phi) = 1 + \epsilon(\cos^2 \phi + \frac{3}{2} \cos^4 \phi). \quad (24)$$

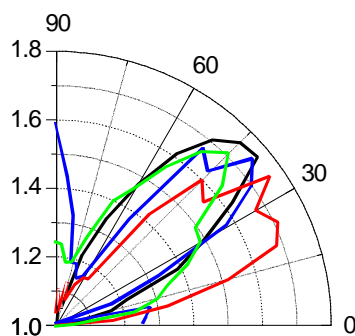


Fig. 33. Farfield emission data for quadrupole-hexadecapole for deformations of $\epsilon = 0.12$ (blue), $\epsilon = 0.16$ (red), $\epsilon = 0.18$ (green), and $\epsilon = 0.2$ (black).

Because the laser operated in the visible ($\lambda \sim 400nm$), it was possible to image the emission from the cavity with conventional optics. The farfield emission data are reproduced in Fig. 5.2. All the deformations above $\epsilon = 0.12$ show a well-localized emission which has approximately the same character over a wide range of deformations. Looking at the SOS of the quadrupole-hexadecapole at $\epsilon = 0.12$, we note that there is a stable orbit - again a triangular one - this time however rotated 90° from the one observed in the quadrupole, with bounce points at $\phi = 0^\circ$ and $\phi = 180^\circ$, at which points the trajectory is incident just above the critical angle for TIR. These are also the points where the maximum emission is emanating from the boundary, according to the imaging data. Unlike the quadrupole lasers then, for this shape there is a stable orbit with bounce points near the critical angle for this deformation and index of refraction and this will support Gaussian modes similar to the bowtie modes seen in the QC laser. An example of such a mode localized on the stable triangular orbit and resulting in emission consistent with the experimental results is shown in Fig. 34.

For this shape, these triangular orbits become unstable above a deformation of $\epsilon = 0.13$, and despite this change, the farfield data don't change in any appreciable way (Fig. 34). Figure 5.2 shows results of calculations for the deformation $\epsilon = 0.16$. The Husimi projection of this mode reveals that it's localized on the triangular periodic orbit, in the vicinity of which complete chaos reigns. Thus, the laser operates on a mode which is based on one and the same classical periodic orbit, insensitive to whether it's stable or unstable.

It's clear from the review of these experiments that lasing modes of cylindrical microresonators need not be based on 'regular' modes such as

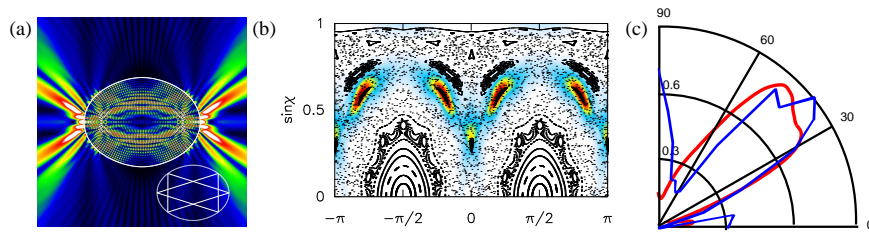


Fig. 34. (a) A numerically calculated mode for a quadrupole-hexadecapolar deformation of $\epsilon = 0.12$ and $n = 2.65$. (b) Husimi projection of the mode in (a). Clearly, the projection is localized on a reflection symmetric pair of stable triangular periodic orbits. (c) The calculated farfield emission pattern.

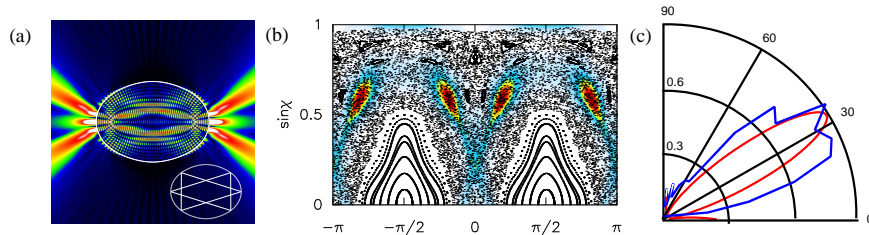


Fig. 35. (a) A numerically calculated mode for a quadrupole-hexadecapolar deformation of $\epsilon = 0.16$ and $n = 2.65$. (b) Husimi projection of the mode in (a). The projection is localized on a triangular orbit of the same geometry as the one in Fig. 5.2, but at this deformation the motion in its vicinity is unstable, leading to chaotic motion. The resulting mode is hence a scarred state. (c) The calculated farfield emission pattern.

stable orbits or whispering gallery modes, but also can get feedback from unstable ray trajectories. It is worth remarking that unstable Fabry-Perot laser resonators have been known since almost the initial conception of the laser^{57,58} and for many purposes are the best design for high-gain laser devices¹⁴ because of their large modal volumes. In ARC microlasers such unstable lasing action arises naturally as one increases the deformation, with the SOS being dominated by more and more chaotic motion. Whether there is any advantage of microlasers based on unstable modes remains to be seen. One crucial point that needs emphasis is that there do exist many complicated chaotic modes which are not related to any single periodic orbit. Indeed in the passive cavity these modes dominate the spectrum as $kR \rightarrow \infty$. However, it may be that the non-linear effects in lasing cavities, either by averaging over fluctuating modes or by mode-locking, enhance the role of modes based on short periodic orbits, whether stable or unstable. It

is striking that all of the experiments on semiconductor ARC lasers can be interpreted as demonstrating lasing from such modes.

6. Unidirectional GaN Spiral microlasers

Since the ARC concept was introduced to obtain directional emission from planar dielectric microlasers one important challenge has been to obtain a single, directed beam out of these devices. As reviewed in previous sections, by using the shape of the resonator as a design parameter it is possible to achieve highly directional emission and other desirable characteristics such as much improved output power. ARC studies, based on smoothly deformed cylindrical resonators, have been supplemented by studies of hexagonal,⁵⁹ triangular,⁶⁰ and square⁶¹ microcavity lasers. However all of these designs were found to emit in multiple directions and exhibit farfield patterns with multiple lobes. In fact it would seem that any lasing mode based on non-normal incidence rays (required for near total internal reflection and hence high-Q) would generate at least two output beams due to the possibility of time-reversed motion on the same trajectory.

Particularly for the development of compact, high power UV emitters, where GaN-based semiconductor compounds are the materials of choice, a planar emitter with uni-directional output coupling is of great interest. Current GaN based lasers use distributed Bragg reflectors (DBRs) in a VCSEL arrangement to achieve high-Q. However DBRs which are also good conductors for the injection current are extremely difficult to fabricate because of the well-known material challenges surrounding the growth of GaN-based layers. Dielectric microcavities can greatly simplify these materials problems associated with GaN-based lasers by using the sidewalls for high-Q feedback while current is fed from the top of the structure. Such structures would of course be planar emitters as opposed to the DBR-based lasers which emit vertically, and would be preferable for most integrated optics applications. However, none of the planar emitters has so far been able to provide a single, directed beam which is a desirable characteristic peculiar to the Fabry-Perot configuration.

Very recently, this difficulty has been overcome with the introduction of spiral-shaped micropillar structures that provide uni-directional emission.¹³ These devices were based on an InGaN multiple quantum-well (MQW) active region, sandwiched between waveguide layers for transverse modal confinement and etched into spiral cross-sections (see Fig. 36), defined by

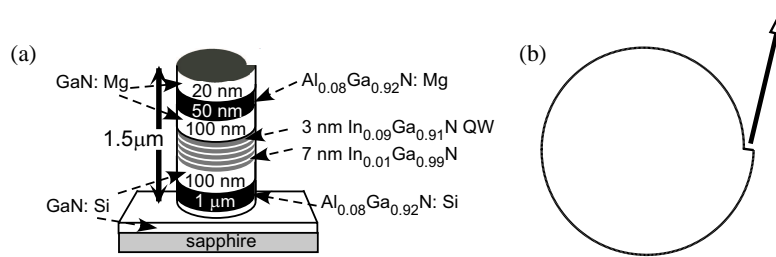


Fig. 36. (a) Structure of the InGaN MQW sample.

the following equation

$$r(\phi) = R_0 \left(1 + \frac{\epsilon}{2\pi} \phi \right) \quad (25)$$

Here ϵ is the deformation parameter, R_0 is the radius of the spiral at $\phi = 0$, and ϕ is measured in radians. This equation implies that the spiral has a discontinuity in radius at $\phi = 0$ where the radius changes abruptly from $r = R_0(1 + \epsilon)$ back to R_0 . Imaging of the emission from the pillar sidewalls shows that the uni-directional emission is from this “notch” (see e.g. inset, Fig. 37(b)). Due to its boundary discontinuity, with a sharp corner on the order of the wavelength at the notch, this structure is not an ARC and is not expected to be well-described by any pure ray-optical description. The discontinuity in the boundary of the spiral at the notch clearly scatters whispering gallery ray trajectories (at least for counter-clockwise rotating waves), and it was not clear in advance that such a structure would support any high-Q modes for lasing. Sharp corners are known to give rise to diffraction, and diffractive effects are in practice thought to be destructive for device performance. As will be explained shortly, the mechanism of this novel design which enables uni-directional out-coupling is primarily based on diffractive effects which couple out a non-emitting (counter-clockwise rotating) WGM.

Initial studies providing the proof of principle were performed under optical pumping conditions. Spirals of various deformations ($\epsilon = 0.05, 0.10$, and 0.15) and sizes ($d = 100 \mu\text{m}, 300 \mu\text{m}$ and $500 \mu\text{m}$) were examined. Results showed lasing of the structures at a wavelength of 404 nm , and that larger sized spirals possess lower thresholds. The spiral with $\epsilon = 0.10$ had the most uni-directional and narrow emission lobe, thus we will focus on the emission characteristics of $\text{In}_{0.09}\text{Ga}_{0.91}\text{N}$ MQWs with $\epsilon = 0.10$ deformation, optically pumped with 355 nm radiation.

Uni-directionality of the observed lasing emission is shown in the farfield image of Fig. 37(b). This polar plot is obtained by integrating over image profiles taken at 5° intervals of the camera angle θ defined such that at $\theta = 0^\circ$ detected emission is normal to the notch (note that this differs from our standard definitions above for which this direction would be $\theta = 90^\circ$ if the notch is along the x-axis). The image field in Fig. 37(a) shows that at $\theta = 30^\circ$, the majority of the emission comes from the spiral notch.

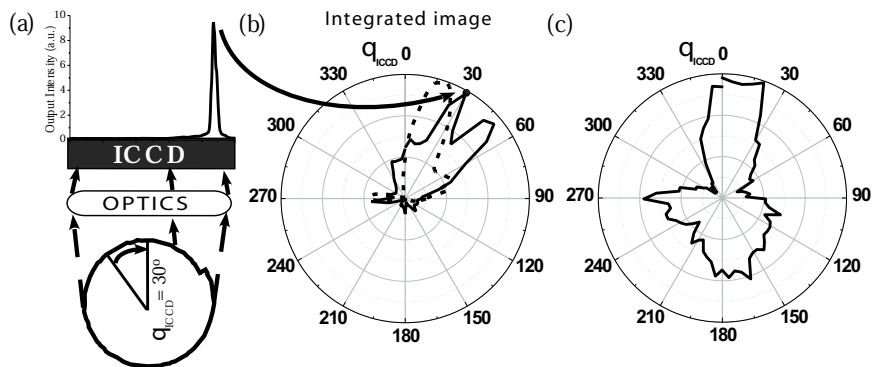


Fig. 37. (a) Image profile of the emission from the spiral microcavity ($\epsilon = 0.10$ and $d = 500 \mu\text{m}$) sidewall at camera angle $\theta = 30^\circ$. Integrating the image profile at each camera angle θ gives (b) uni-directional farfield pattern of the spiral. Experimental data (solid line) are in good agreement with numerical calculation (dotted line). (c) Farfield pattern obtained when the spiral cavity is pumped uniformly.

A crucial feature in the success of spiral lasers is the *selective pumping method* employed. Based on previous experiments⁶² on circular micropillars, which have shown that lower thresholds can be attained by a spatially selective pumping of the microcavity, the spiral cavities were optically excited using an axicon lens to form a ring shaped beam. The aim was to achieve an optimal overlap with the high-Q mode, following theoretical results which show that the spiral resonator supports long-lived modes confined close to the perimeter. This also serves to *suppress* other unwanted modes and scattering from the discontinuity, which then are dissipated due mainly to the absorption of the material. The effectiveness of selective pumping method is demonstrated in Fig. 37(c), which shows a broad emission pattern under uniform pumping conditions. The spatial disposition of the numerically calculated high-Q modes together with the results of the selective pumping method can be exploited in the design of the electrodes under current

injection conditions to optimize the emission.

Numerical calculations show that there are indeed such dominantly notch-emitting quasi-bound states of the spiral microcavity. Figure 38(a) plots the modulus of the electric field of such a resonance in real-space, showing that it is concentrated close to the boundary and exhibiting properties associated with a WG-like mode. However, these modes display a crucial difference from the regular WG-modes of a circular resonator: the high-Q resonances of the spiral exhibit a pronounced *chirality* and are predominantly composed of clockwise rotating components (corresponding to ray motion which could not escape at the notch). This can be easily deduced from the decomposition of the mode into its circular harmonics

$$E(\mathbf{r}) = \sum_{m=-\infty}^{+\infty} \alpha_m J_m(r) e^{im\varphi} \quad (26)$$

given in Fig. 38(b).

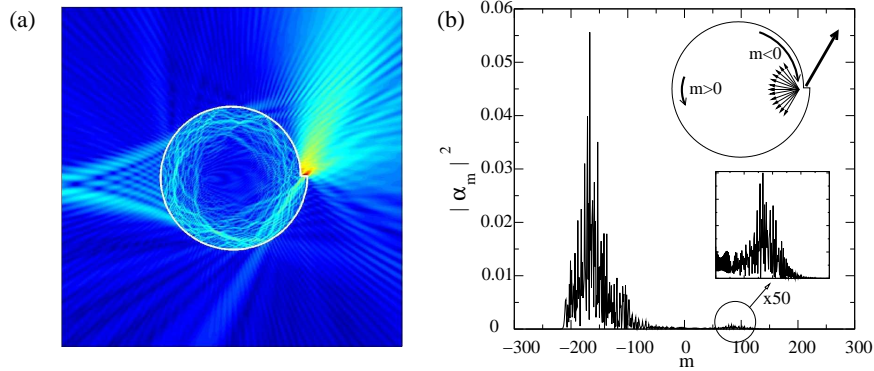


Fig. 38. (a) Real-space false color plot of the modulus of the electric field for a calculated quasi-bound state at $nkRo \approx 200$ at $\epsilon = 0.10$ deformation. (b) Distribution of angular momenta for the resonance plotted in (a). Note the peak at negative m corresponding to clockwise rotation (see inset) and the small weight at positive m which constitute the diffracted waves emitting from the notch.

Interpreting each component m in the sum as representing ray motion incident on the boundary at an angle of incidence $\sin \chi = m/nkR$ in the short-wavelength limit, we get a distribution of incidence angles. The strong weighting of the distribution to negative components ($-m$) peaked around $|m| \approx 160$ corresponds to a mode with mostly clockwise-rotating waves having angle of incidence $\sin \chi \approx 0.8$ and which are hence totally internally

reflected (the critical angle χ_c is defined by $\sin \chi_c = \pm \frac{1}{n} = \pm 0.38$ for $n = 2.6$). Such a stationary distribution is counter-intuitive from the point of view of ray dynamics inside this spiral shaped dielectric billiard. Ray simulations show that if we start a ray bundle which is predominantly composed of clockwise rotating rays close to the boundary ($\sin \chi \approx -1$), the average impact angle diffuses monotonically towards 0, where the rays strike the boundary at normal incidence, and further towards positive $\sin \chi$ (see Fig. 39).

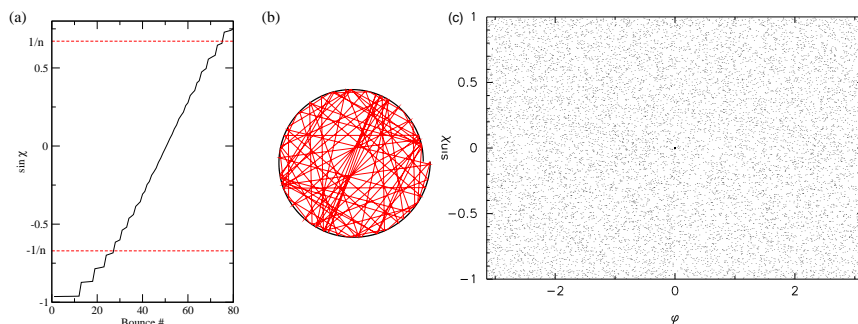


Fig. 39. (a) The diffusion of a ray started at $\varphi = 2\pi - 0.01, \sin \chi = -0.96$. At the uppermost point of the curve, the ray leaves the resonator from the notch, (b) the trajectory plotted in real-space, (c) surface of section of the spiral with $\varepsilon = 0.1$.

For a dielectric billiard, the intensity would then refract out at some point away from the notch long before it can reverse its sense of rotation. Furthermore, there are no periodic orbits whose bounce points are entirely on the smooth portions of the boundary, simply because the curvature is monotonic. This is clear e.g. for the bouncing ball orbit as due to the monotonic curvature there exist no two points on the boundary with colinear and opposite normal vectors. More generally any periodic orbit would have to have pairs of bounces for which $\Delta \sin \chi$ has both signs, whereas the monotonic variation in $\sin \chi$ away from the notch does not permit this. Therefore the only periodic orbits of this billiard have at least one bounce point on the notch area. Their associated islands of stability are quite small as shown by the surface of section in Fig. 39 which appears completely chaotic. Modes based on such long periodic orbits are rarely important. If they are unstable they are unlikely to have strong scars for the reasons discussed in the previous section; if they are stable the islands of stability are typically very small and the resulting modes have small mode volumes. More impor-

tantly, our numerical calculations on the passive cavity indicate no weight in the emitting mode near zero angular momentum, which cannot happen for periodic orbits in this structure.

In systems where periodic orbits are rare, diffractive contributions can be significant. It's known for instance from the study of open microwave resonators, that in the regime where there are no stable periodic orbits, orbits that diffract off the sharp edges of the resonator can have a strong influence on the spectrum and wavefunctions.⁶³ Similarly, the analysis of the spiral billiard suggests that for the formation of a notch-emitting high-Q mode, a mechanism beyond geometric optics (such as diffraction) is necessary. If a wavepacket of cylindrical waves with dominantly negative components were injected into the system, the notch, which is discontinuous on the scale of a wavelength, would diffract a small part of the amplitude into positively rotating components above the critical angle, which would eventually be emitted from the notch. Hence we interpret the small amount of counter-clockwise (ccw) rotating waves found numerically as responsible for emission at the notch; and these components are due to diffraction of the clockwise-waves as they pass the inner corner of the notch (see inset Fig. 38(b)). Attempts to reproduce the experimental emission patterns with any reasonable initial ray bundle that only reflects specularly (and refracts out according to Snell's Law) fail to reproduce the observed emission behavior for the reasons alluded to above: clockwise ray bundles escape through the smooth part of the boundary by refraction before they reverse direction, solely counter-clockwise ray bundles do escape from the notch but would correspond to an unphysically low Q-value (and contradict wave solutions). Therefore we believe diffraction effects are crucial to the uni-directional lasing from this device.

Another counter-intuitive feature of the experimental results is that the farfield emission lobe is not maximum at $\theta_{ICCD} = 0^\circ$ corresponding to normal emission from the notch, but has two "lobes" peaked at the angles: $\theta_{ICCD} \approx 30^\circ$ and $\theta_{ICCD} \approx 50^\circ$ (see Fig. 37(b)). This tilt in the vicinity of the notch arises because the ccw-component of the resonance cannot be viewed as a Gaussian beam incident on the notch interface; instead there is a distribution of wavevectors determined by the specific resonance. By an angular decomposition of the incident field on the notch, we can numerically propagate it to the farfield.

We assume first that the emitting (part of the) mode is composed of a single angular momentum component, which is a reasonable starting point given that the distribution of the positive components in the numerically

calculated quasi-bound states is narrow, and becomes narrower for higher wavenumbers. Let the notch interface be at $z = 0$. At the interface, infinitesimally below it, the angular spectrum of the field can be expressed as

$$\tilde{\Psi}(z = 0^-, s) = \int_0^\infty dx J_m(nkx) e^{-inksx} \quad (27)$$

Then we can write

$$\Psi(z = 0^+, x) = \int_{-\infty}^\infty t(s) \tilde{\Psi}(z = 0^-, s) e^{iksx} \quad (28)$$

So that if we propagate this field to points $z > 0$

$$\Psi(z > 0, x) = \int_{-\infty}^\infty t(s) \tilde{\Psi}(z = 0^-, s) e^{ik(sx + \sqrt{1-s^2}z)} \quad (29)$$

Consider the transform in Eq. (27). Only part of the incident radiation will be incident on the notch interface, so we change the limits of the integral accordingly. Scaling the variables inside the integral as well, we get:

$$\tilde{\Psi}(s) = \frac{1}{nk} \int_{nkR_0}^{nkR_0(1+\epsilon)} d\tilde{x} J_m(\tilde{x}) e^{-is\tilde{x}}. \quad (30)$$

In this way, the size scale of the notch (with respect to the wavelength) enters the calculation. Calculating the field asymptotically at infinity, we obtain after a saddle point calculation:⁵⁶

$$I(\theta) \propto \left| \frac{\sqrt{n^2 - \sin^2 \theta} \cos \theta}{\sqrt{n^2 - \sin^2 \theta} + n\sqrt{1 - \sin^2 \theta}} \tilde{\Psi}\left(\frac{\sin \theta}{n}\right) \right|^2 \quad (31)$$

The results in Fig. 40(a) show a fluctuating emission pattern with no strong directional peak when $R_c = m/nk \ll R_0$, i.e. the caustic of the emitting circular wave is between the edge of the notch at $\phi = 0, r = R_0$ and the origin. Directional emission sets in as the caustic approaches the notch and a single (though rather broad) peak results, which is displaced from the normal direction. The angular displacement from the notch normal vanishes as the mode intensity moves fully into the notch area and becomes confined closer to the outer rim $r = R_0(1+\epsilon)$, as expected from rays incident increasingly at normal angles to the notch interface.

Finally, it is possible to check whether this asymptotic propagation method gives a good representation of the actual farfield by calculating the farfield emission profile of the numerically calculated internal mode in Fig. 38 using Eq. (31). The result is shown in Fig. 40(b), and is in

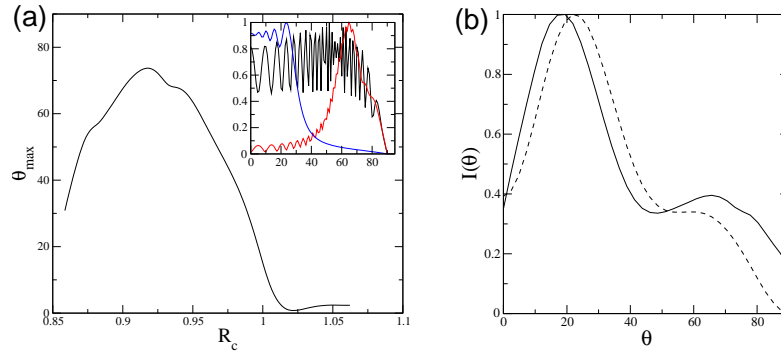


Fig. 40. (a) The variation of the angular shift of the peak emission from the notch with the position of the caustic of the counterclockwise rotating cylindrical wave (smoothed). Inset samples the behavior of the field in the farfield for three values of R_c ; $R_c = 0.86$ (black), $R_c = 0.95$ (red) and $R_c = 1.05$ (blue). All intensities are scaled to be 1 at maximum. The calculations are performed for the experimental size parameter $nkR \approx 9300$. (b) Comparison of the numerically calculated farfield for the resonance in Fig. 38 (solid curve) and the propagated farfield (cf. Eq. (31)) (dashed curve).

good agreement with the numerically determined farfield. The reliability of Eq. (31) of course is better the higher the size parameter nkR .

If a diffractive mechanism is responsible for the uni-directional emission from the notch of the spiral resonator then the output characteristics are expected to be sensitive to the shape and sharpness of the notch. Further experiments and modeling are required to see if this is the case. It remains possible that a rather different physical picture of the lasing mode will emerge under further study. For example a “ray model” of diffraction, based on isotropic diffraction from the corner of the notch does not reproduce the experimental behavior. This suggests that there are additional physical effects which allow this device to perform as well as it does; we hope to elucidate these mechanisms through further research.

Very recently new experiments have been performed in a PARC-Yale collaboration on spiral-shaped InGaN MQW lasers with electrical injection pumping demonstrating low current thresholds and output power of more than 25mw at 400nm.⁶⁴ The heterostructure used was identical to the one reported in the above work. The design (placement and shape) of the electrode on the top-face of the p-GaN layer, which we pointed out is an important issue, followed the results of the optical injection investigation. It is to be noted that while selective optical pumping is limited to having simple shapes, e.g., in the form of a ring or a line at various tilt angles, se-

lective injection current pumping can have rather complex designs simply by incorporating the shape complexities in the mask design, e.g., designing the opaque electrode patterned after the perimeter of the notch. Future work is expected to make optimal use of this technique in more complex scenarios.

In conclusion, the work summarized in this section demonstrates that the spiral geometry is a viable design of GaN-based laser devices for integrated optical applications.

7. Summary and outlook

A wide range of experiments combined with ray and wave modeling has shown that non-symmetric dielectric microresonators and lasers have a rich set of properties. Low index ARC lasers and resonators are remarkably well described by ray escape models based on flow patterns in partially chaotic phase space. Semiconductor ARCs show interesting lasing effects based on short periodic orbits. Basic phenomena of interest in the field of quantum/wave chaos are observed, such as chaos-assisted tunneling and scarring. Classical concepts such as the unstable and stable non-linear manifolds of periodic orbits lie at the heart of the observed directional emission in low index ARCs, which occurs despite the presence of strong chaos. The semiconductor ARC and spiral lasers are typically not well-described by ray models but still can be analyzed fruitfully by looking at the high-Q modes in the ray phase space.

From the point of view of applications these non-symmetric dielectric resonators have shown two striking advantages. First, at least in the case of the quantum cascade ARC lasers, deformation from a symmetric boundary shape led to an enormous increase in output efficiency. Second, for the spiral laser, chiral whispering gallery modes appear to provide both relatively high Q and uni-directional emission. This is of particular importance for the GaN-based blue and UV lasers for which conventional approaches are difficult or impossible to implement at the same size scale. It is hoped that during the next period of research and development of asymmetric resonant cavities these promising device characteristics will allow such cavities to become part of useful technologies.

8. Acknowledgments

We would like to acknowledge the contributions to this research by our collaborators. On the theory side these include Jens Nöckel, Evgenii Nari-

manov, Gregor Hackenbroich and Philippe Jacquod. On the experimental side these include Nathan Rex, Grace Chern, Andrew Poon and Seongsik Chang from Yale, Tahar Ben Massoud and Joseph Zyss from ENS Cachan, Noble Johnson and Michael Kneissl from PARC, Lou Guido from Virginia Polytechnic and Claire Gmachl and Federico Capasso from Bell Labs. Various aspects of the research here were supported by NSF grants DMR - 008541, PHY - 9612200, AFOSR (F49620-00-1-0182), DARPA SUVOS program under SPAWAR systems grant No. N666001-02-C-8017. We thank Scott Lacey and Jens Nöckel for providing us with figures and calculations related to the research of Ref. 28.

References

1. Y. Yamamoto and R. E. Slusher. Optical processes in microcavities. *Phys. Today*, 46:66–73, 1993.
2. R. K. Chang and A. K. Campillo, editors. *Optical Processes in Microcavities*. World Scientific, Singapore, 1996.
3. Kerry J. Vahala. Optical microcavities. *Nature*, 424:839–846, 2003.
4. J. U. Nöckel, A. D. Stone, and R. K. Chang. Q-spoiling and directionality in deformed ring cavities. *Opt. Lett.*, 19:1693–1695, 1994.
5. J. U. Nöckel and A. D. Stone. *Chaotic Light: a theory of asymmetric cavity resonators*, chapter 11, pages 389–426. World Scientific, Singapore, 1996.
6. A. D. Stone. Wave-chaotic optical resonators and lasers. *Phys. Scr.*, T90:248–262, 2001.
7. C. Gmachl, F. Capasso, E. E. Narimanov, J. U. Nöckel, A. D. Stone, J. Faist, D. L. Sivco, and A. Y. Cho. High-power directional emission from microlasers with chaotic resonators. *Science*, 280:1556–1564, 1998.
8. S. Gianordoli, L. Hvozdar, G. Strasser, W. Schrenk, J. Faist, and E. Gornik. Long-wavelength $\lambda = 10\mu\text{m}$ quadrupolar-shaped gaas-algaas microlasers. *IEEE J. Quantum Electron.*, 36:458–464, 2000.
9. C. Gmachl, E. E. Narimanov, F. Capasso, J. N. Baillargeon, and A. Y. Cho. Kolmogorov-arnold-moser transition and laser action on scar modes in semiconductor diode lasers with deformed resonators. *Opt. Lett.*, 27:824–826, 2002.
10. N. B. Rex. *Regular and chaotic orbit Gallium Nitride microcavity lasers*. PhD thesis, Yale University, 2001.
11. N. B. Rex, H. E. Tureci, H. G. L. Schwefel, R. K. Chang, and A. D. Stone. Fresnel filtering in lasing emission from scarred modes of wave-chaotic optical resonators. *Phys. Rev. Lett.*, 88:art. no. 094102, 2002.
12. Harald G. L. Schwefel, Nathan B. Rex, Hakan E. Tureci, Richard K. Chang, A. Douglas Stone, and Joseph Zyss. Dramatic shape sensitivity of directional emission patterns from similarly deformed cylindrical polymer lasers. *submitted to JOSA B*, 2003.
13. G. D. Chern, H. E. Tureci, A. D. Stone, R. K. Chang, M. Kneissl, and

- N. M. Johnson. Unidirectional lasing from ingan multiple-quantum-well spiral-shaped micropillars. *Applied Physics Letters*, 83:1710–1712, 2003.
14. A. E. Siegman. *Lasers*. University Science Books, Mill Valley, California, 1986.
 15. H. E. Tureci, H. G. L. Schwefel, A. D. Stone, and E. E. Narimanov. Gaussian-optical approach to stable periodic orbit resonances of partially chaotic dielectric micro-cavities. *Opt. Express*, 10:752–776, 2002.
 16. J. B. Keller and S. I. Rubinow. Asymptotic solution of eigenvalue problems. *Ann. Phys.*, 9:24–75, 1960.
 17. V. M. Babić and V. S. Buldyrev. *Asymptotic Methods in Shortwave Diffraction Problems*. Springer, New York, USA, 1991.
 18. H. E. Tureci, H. G. L. Schwefel, Ph. Jacquod, and A. Douglas Stone. Modes of wave-chaotic dielectric resonators. submitted to *Progress in Optics*.
 19. A. Einstein. Zum quantensatz von sommerfeld und epstein. *Verhandl. Deut. Physik. Ges.*, 19:82–92, 1917.
 20. Hakan E. Türeci. *Wave chaos in dielectric resonators: Asymptotic and numerical approaches*. PhD thesis, Yale University, 2003.
 21. L. E. Reichl. *The transition to chaos in conservative classical systems: quantum manifestations*. Springer, New York, USA, 1992.
 22. V. I. Arnold. *Mathematical methods of classical mechanics*. Springer, New York, USA, 1989.
 23. V. F. Lazutkin. *KAM theory and semiclassical approximations to eigenfunctions*. Springer, New York, USA, 1993.
 24. A. J. Lichtenberg and M. A. Leiberman. *Regular and chaotic dynamics*. Springer, New York, USA, 1992.
 25. E. Doron and U. Smilansky. Semiclassical quantization of chaotic billiards - a scatteringtheory approach. *Nonlinearity*, 5:1055–1084, 1992.
 26. B. Dietz, J. P. Eckmann, C. A. Pillet, U. Smilansky, and I. Ussishkin. Inside-outside duality for planar billiards - a numerical study. *Phys. Rev. E*, 51:4222–4231, 1995.
 27. K. Husimi. Some formal properties of the density matrix. *Proc. Phys. Math. Soc. Jpn.*, 22:264–314, 1940.
 28. S. Lacey, H. Wang, D. H. Foster, and J. U. Nöckel. Directional tunnel escape from nearly spherical optical resonators. *Phys. Rev. Lett.*, 91:033902, 2003.
 29. J. W. Goodman. *Introduction to Fourier Optics*. Mc Graw-Hill, New York, USA, 1996.
 30. J. U. Nöckel, A. D. Stone, G. Chen, H. L. Grossman, and R. K. Chang. Directional emission from asymmetric resonant cavities. *Opt. Lett.*, 21:1609–1611, 1996.
 31. J. U. Nöckel and A. D. Stone. Ray and wave chaos in asymmetric resonant optical cavities. *Nature*, 385:45–47, 1997.
 32. M. Robnik and M. V. Berry. Classical billiards in magnetic-fields. *J. Phys. A-Math. Gen.*, 18:1361–1378, 1985.
 33. S. Chang, R. K. Chang, A. D. Stone, and J. U. Nöckel. Observation of emission from chaotic lasing modes in deformed microspheres: displacement by the stable-orbit modes. *J. Opt. Soc. Am. B-Opt. Phys.*, 17:1828–1834, 2000.

34. S. Chang, N. B. Rex, R. K. Chang, G. B. Chong, and L. J. Guido. Stimulated emission and lasing in whispering gallery modes of gan microdisk cavities (vol 75, pg 166, 1999). *Appl. Phys. Lett.*, 75:3719–3719, 1999.
35. H. E. Tureci, H. G. L. Schwefel, Ph. Jacquod, and A. Douglas Stone. Modes of wave-chaotic dielectric resonators. submitted to *Progress in Optics*.
36. H. Poritsky. The billiard ball problem on a table with convex boundary - an illustrative dynamical problem. *Annals of Mathematics*, 51:446 – 470, 1950.
37. Edoh Y. Amiran. Integrable smooth planar billiards and evolutes. *New York J. Math.*, 3:32–47, 1997.
38. S. Smale. Differentiable dynamical systems. *Bull. Amer. Math. Soc.*, 73:747–817, 1967.
39. J. U. Nöckel. *Resonances in nonintegrable open systems*. PhD thesis, Yale University, 1997.
40. A. Mekis, J. U. Nöckel, G. Chen, A. D. Stone, and R. K. Chang. Ray chaos and q spoiling in lasing droplets. *Phys. Rev. Lett.*, 75:2682–2685, 1995.
41. S. Chang, R. K. Chang, A. D. Stone, and J. U. Nöckel. Observation of emission from chaotic lasing modes in deformed microspheres: displacement by the stable-orbit modes. *J. Opt. Soc. Am. B-Opt. Phys.*, 17:1828–1834, 2000.
42. S. B. Lee, J. H. Lee, J. S. Chang, H. J. Moon, S. W. Kim, and K. An. Observation of scarred modes in asymmetrically deformed microcylinder lasers. *Phys. Rev. Lett.*, 8803:art. no. 033903, 2002.
43. F. Capasso, C. Gmachl, D. L. Sivco, and A. Y. Cho. Quantum cascade lasers. *Phys. Today*, 55:34–40, 2002.
44. L. A. Lugiato, C. Oldano, and L. M. Narducci. Cooperative frequency locking and stationary spatial structures in lasers. *Journal Of The Optical Society Of America B-Optical Physics*, 5:879–888, 1988.
45. V. Zehnlé. Theoretical analysis of a bimode laser. *Physical Review A*, 57:629–643, 1998.
46. C. Tamm. Frequency locking of 2 transverse optical modes of a laser. *Physical Review A*, 38:5960–5963, 1988.
47. S. Gianordoli, L. Hvozdará, G. Strasser, W. Schrenk, J. Faist, and E. Gornik. Long-wavelength ($\lambda=10\ \mu\text{m}$) quadrupolar-shaped gaas-algaas micro-lasers. *IEEE J. Quantum Electron.*, 36:458–464, 2000.
48. V. A. Podolskiy and E. E. Narimanov. Universal level-spacing distribution in quantum systems. preprint server nlin.CD/0310034.
49. M. J. Davis and E. J. Heller. Quantum dynamical tunneling in bound-states. *J. Chem. Phys.*, 75:246–254, 1981.
50. E. E. Narimanov. Private Communication, October 2003.
51. E. J. Heller. Bound-state eigenfunctions of classically chaotic hamiltonian-systems - scars of periodic-orbits. *Phys. Rev. Lett.*, 53:1515–1518, 1984.
52. L. Kaplan and E. J. Heller. Linear and nonlinear theory of eigenfunction scars. *Ann. Phys.*, 264:171–206, 1998.
53. L. Kaplan. Scars in quantum chaotic wavefunctions. *Nonlinearity*, 12:R1–R40, 1999.
54. M. V. Berry. Regular and irregular semiclassical wavefunctions. *J. Phys. A-Math. Gen.*, 10:2083–2091, 1977.

55. E. B. Bogomolny. Smoothed wave-functions of chaotic quantum-systems. *Physica D*, 31:169–189, 1988.
56. H. E. Tureci and A. D. Stone. Deviation from snell's law for beams transmitted near the critical angle: application to microcavity lasers. *Opt. Lett.*, 27:7–9, 2002.
57. A. E. Siegman. Laser beams and resonators: The 1960s. *IEEE J. Sel. Top. Quantum Electron.*, 6:1380–1388, 2000.
58. A. E. Siegman. Laser beams and resonators: Beyond the 1960s. *IEEE J. Sel. Top. Quantum Electron.*, 6:1389–1399, 2000.
59. I. Braun, G. Ihlein, F. Laeri, J. U. Nöckel, G. Schulz-Ekloff, F. Schuth, U. Vietze, O. Weiss, and D. Wöhrle. Hexagonal microlasers based on organic dyes in nanoporous crystals. *Appl. Phys. B-Lasers Opt.*, 70:335–343, 2000.
60. Y. Z. Huang, W. H. Guo, and Q. M. Wang. Influence of output waveguide on mode quality factor in semiconductor microlasers with an equilateral triangle resonator. *Appl. Phys. Lett.*, 77:3511–3513, 2000.
61. A. W. Poon, F. Courvoisier, and R. K. Chang. Multimode resonances in square-shaped optical microcavities. *Opt. Lett.*, 26:632–634, 2001.
62. N. B. Rex, R. K. Chang, and L. J. Guido. Threshold lowering in gan micropillar lasers by means of spatially selective optical pumping. *IEEE Photonics Technol. Lett.*, 13:1–3, 2001.
63. J. S. Hersch, M. R. Haggerty, and E. J. Heller. Diffractive orbits in an open microwave billiard. *Phys. Rev. Lett.*, 83:5342–5345, 1999.
64. M. Kneissl, M. Teepe, N. Miyashita, N. M. Johnson, G. D. Chern, and R. K. Chang. Current-injection spiral-shaped microcavity disk laser diodes with uni-directional emission. submitted to ...

INDEX

- Adiabatic invariant curves, 35
- ARC Microlasers
 - GaN, 56–67
 - polymer, 26
 - quantum cascade, 48–55
- Asymmetric Resonant Cavity (ARC)
 - low-index, 25–47
 - semiconducting, 47–67
- Billiards, 2, 7, 12, 25
 - ellipse, 10, 12, 26, 27, 29, 33
 - quadrupole, 13–16, 20, 27, 29, 35, 49, 53, 57
 - quadrupole-hexadecapole, 28, 29, 64
 - Quantum, 2, 25
- Boundary image field, 24
- bowtie modes, 12, 49–53, 56
- Caustics
 - elliptic, 8
 - hyperbolic, 10
- Chaos, 2
 - Quantum chaos, *see* Quantum chaos (chaotic) systems
 - Ray chaos, *see* Ray chaos
 - Wave chaos, *see* Wave chaos (chaotic) systems
- Chaos-assisted tunneling, 55–56
- Dynamical eclipsing, 28, 33–36
- Dynamical tunneling, 55
- EBK method, 9
- Eikonal
 - applied to ellipse, 8
 - equation, 6
 - failure of, 5–9
 - theory, 4–9
- Einstein, 5, 9
- Farfield pattern, 24
- Fresnel filtering, 62–63
- Gaussian optics
 - in ARCs, 4, 5, 9, 51–53
 - Q-values of, 55–56
 - quantization rule, 10, 51
 - relation to eikonal method, 9
 - stable periodic orbit modes, 5, 51
- Husimi projection, 18–22
- Husimi-SOS projection, 19
- Image field, 22–25
- Integrable vs. mixed dynamics, 9, 12
- Invariant curves, 13, 14, 20, 31
 - Adiabatic, *see* Adiabatic invariant curves
- Kolmogorov-Arnold-Moser (KAM)
 - tori, 9, 13
 - transition, 12
- Monodromy or stability matrix, 37
- Open vs. closed resonator, 15
- Quantum chaos (chaotic) systems, 2, 4, 9

Index

81

- Ray chaos, 2, 9, 12–16
- Ray dynamics, 12–16

- Scarred modes, 3, 57
 - in GaN lasers, 56–62
 - theory of, 60–62
- Silica microresonators, 43–47
- Spiral Laser
 - chiral WG modes, 70
 - diffraction effects in, 72, 74
 - ray dynamics of, 70–72
 - uni-directional emission, 67
- Spiral microlasers, 48, 67–75
- Stable and unstable manifolds, 36–40

- Wave chaos (chaotic) systems, 2–79
- Whispering gallery modes, 2, 20, 25, 33–36, 64, 68, 70